Bioactive Materials 44 (2025) 544–557

Contents lists available at ScienceDirect

Bioactive Materials

journal homepage: www.keaipublishing.com/en/journals/bioactive-materials

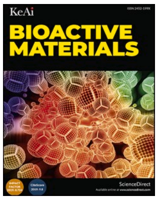

Innovative spiral nerve conduits: Addressing nutrient transport and cellular activity for critical-sized nerve defects

Allen Zennifer [a,c], S.K. Praveenn Kumar [a], Shambhavi Bagewadi [a], Swathi Unnamalai [a], Davidraj Chellappan [b], Sama Abdulmalik [c], Xiaojun Yu [d], Swaminathan Sethuraman [a], Dhakshinamoorthy Sundaramurthi [a,**], Sangamesh G. Kumbar [c,*]

[a] *Tissue Engineering & Additive Manufacturing (TEAM) Lab, Centre for Nanotechnology & Advanced Biomaterials, School of Chemical & Biotechnology, SASTRA Deemed University, Tamil Nadu, India*
[b] *Central Animal Facility (CAF), School of Chemical & Biotechnology, SASTRA Deemed University, Tamil Nadu, India*
[c] *Department of Orthopedic Surgery, University of Connecticut Health Center, 263 Farmington Avenue, Farmington, CT, 06030-4037, USA*
[d] *Department of Biomedical Engineering, Stevens Institute of Technology, 1 Castle Point on Hudson Hoboken, New Jersey, 07030, USA*

ARTICLE INFO

Keywords:
Nerve guide conduits
Spiral micro-nanostructures
Large-gap nerve defect
Poly(3-hydroxybutyrate-co-3-hydroxy valerate) (PHBV)
Thermoplastic polyurethane (TPU)

ABSTRACT

Large-gap nerve defects require nerve guide conduits (NGCs) for complete regeneration and muscle innervation. Many NGCs have been developed using various scaffold designs and tissue engineering strategies to promote axon regeneration. Still, most are tubular with inadequate pore sizes and lack surface cues for nutrient transport, cell attachment, and tissue infiltration. This study developed a porous spiral NGC to address these issues using a 3D-printed thermoplastic polyurethane (TPU) fiber lattice. The lattice was functionalized with poly(3-hydroxybutyrate-co-3-hydroxyvalerate) (PHBV) electrospun aligned (aPHBV) and randomly (rPHBV) oriented nanofibers to enhance cellular activity. TPU lattices were made with 25 %, 35 %, and 50 % infill densities to create scaffolds with varied mechanical compliance. The fabricated TPU/PHBV spiral conduits had significantly higher surface areas (25 % TPU/PHBV: 698.97 mm^2, 35 % TPU/PHBV: 500.06 mm^2, 50 % TPU/PHBV: 327.61 mm^2) compared to commercially available nerve conduits like Neurolac™ (205.26 mm^2). Aligned PHBV nanofibers showed excellent Schwann cell (RSC96) adhesion, proliferation, and neurogenic gene expression for all infill densities. Spiral TPU/PHBV conduits with 25 % and 35 % infill densities exhibited Young's modulus values comparable to Neurotube® and ultimate tensile strength like acellular cadaveric human nerves. A 10 mm sciatic nerve defect in Wistar rats treated with TPU/aPHBV NGCs demonstrated muscle innervation and axon healing comparable to autografts over 4 months, as evaluated by gait analysis, functional recovery, and histology. The TPU/PHBV NGC developed in this study shows promise as a treatment for large-gap nerve defects.

1. Introduction

Peripheral nerve injuries (PNI) primarily occur due to laceration, contusion, gunshot wounds, traction, systemic diseases like diabetes, and autoimmune disorders like rheumatoid arthritis, leading to distortions in nerve anatomy [1]. The annual global incidence of traumatic peripheral nerve injuries in developed countries has been estimated to be approximately 13–23 per 100,000 population [2]. Peripheral nerves possess the innate ability to heal, but at a slow rate of 1 mm/day, making it challenging to repair critical-sized injuries greater than 4 cm in humans [3] Autografts are often preferred for smaller defects due to their higher healing potential. However, they have several limitations, including the need for secondary surgery, donor site morbidity, limited tissue availability in size and structure, and the risk of neuroma formation. Acellular allografts or xenografts, while available, are not ideal for large-gap (>4 cm) peripheral nerve injury (PNI) repair and face

---

Peer review under responsibility of KeAi Communications Co., Ltd.

* Corresponding author. Department of Orthopedic Surgery, Department of Biomedical Engineering, Department of Materials Science and Engineering, University of Connecticut Health Center, 263 Farmington Avenue, Farmington, CT-06030, USA.

** Corresponding author. Tissue Engineering & Additive Manufacturing (TEAM) Lab, Centre for Nanotechnology & Advanced Biomaterials (CeNTAB), School of Chemical & Biotechnology, SASTRA Deemed University, Tirumalaisamudram, Thanjavur, 613 401, Tamilnadu, India.

E-mail addresses: dhakshinamoorthy@scbt.sastra.edu (D. Sundaramurthi), kumbar@uchc.edu (S.G. Kumbar).

https://doi.org/10.1016/j.bioactmat.2024.10.028
Received 27 October 2024; Accepted 31 October 2024

challenges such as immune reactions and inconsistent healing outcomes [4].

Engineered nerve guidance conduits (NGCs) are designed to address unmet clinical needs in the repair of large-gap nerve defects. Various micro- and nanofabrication techniques, such as molding, salt leaching, 3D printing, and electrospinning, have been employed to create these scaffolds [5–12]. A wide range of natural and synthetic biomedical polymers have been used to develop engineered NGCs that structurally mimic nerves and provide bioactivity [5–12]. FDA-approved NGCs, such as Avance Nerve Graft®, Axoguard Nerve Connector®, and NeuraGen®, are typically tubular conduits made from natural biomaterials or synthetic materials [13]. While these conduits have shown positive outcomes for small-sized nerve lesions, they often lack the bioactivity and biochemical cues necessary for effective repair of large-gap nerve defects [14]. Engineered NGCs have been enhanced with intraluminal fillers (hydrogels and xerogels), multi-channel designs, cells, extracellular matrix proteins, neurotrophic factors, and controlled release systems to promote nerve regeneration [15–18]. Although these engineered NGCs offer improved healing outcomes, their adoption for manufacturing remains challenging due to complex and time-consuming fabrication processes [5]. Efforts are underway to combine micro- and nanofabrication techniques to develop NGCs with synergistic features that enhance nerve healing [19]. For instance, melt electrowriting and electrospinning techniques have been used to create conductive, multiscale-filled NGCs featuring both micro- and nanostructures [20]. The outer layer of these NGCs consists of electrospun random PCL/collagen nanofibers (500 nm), which act as a barrier to prevent fibroblast infiltration while remaining permeable to nutrients. The intermediate layer contains PCL and reduced graphene oxide (rGO) composite microfibers, approximately 125 μm in size, providing conductivity and mechanical strength. Additionally, ~10 μm-sized melt electrowritten PCL microfibers are aligned longitudinally to promote neural cell growth along the fibers [20]. While multi-scaled NGCs offer appealing designs, their fabrication is complex and often lacks the necessary mechanical strength for large-gap nerve repair. The tensile and compressive loads these NGCs can withstand typically range from 0.5 to 1.5 N, comparable to many biological allografts used for small-sized nerve defects [21,22].

In this study, we developed NGCs using a combination of fused deposition modeling (FDM) and electrospinning to achieve mechanical stability and nanofibrous cues, addressing the limitations identified by Fang *et al.*, [20]. Our spiral-structured NGC significantly enhances the inner lumen surface area compared to traditional tubular NGCs, promoting better transport features and axon regeneration. We utilized FDA-approved polymeric excipients, including thermoplastic polyurethane (TPU) [23,24] and poly(3-hydroxybutyrate-co-3-hydroxyvalerate) (PHBV) [25,26] to create this spiral micro-nanostructured NGC. These materials were selected for their unique physicochemical properties and biocompatibility. Unlike polyesters such as PCL, PLA, and PGA, TPU offers tunable properties by adjusting its hard segments (e.g., isocyanates) and soft segments (e.g., polyols), which influence mechanical strength and degradation rates [27]. The PHBV nanofibers coated on the implant provide anchorage and directional guidance for regenerating axons, while their piezoelectric properties are expected to enhance nerve regeneration *in vivo* [28].

Electrospinning is a versatile technique for developing micro and nanofibers with various alignments [29–31]. These ECM-mimicking fiber matrices have been explored for neural tissue engineering due to their ability to enhance cell adhesion, migration, proliferation, and contact guidance for regenerating axons [10]. However, these matrices generally suffer from reduced porosity and poor mechanical strength [32], which may not be optimal for large nerve regeneration. FDM is a 3D printing method that produces continuous microfilaments from the molten thermoplastic polymers including PLA and TPU. The microfabrication 3D printing technique has been adopted to print biomedical implants using metals [33], polymers [34], and composites [35].

We hypothesized that the 3D-printed micro-structured TPU fiber lattice would provide mechanical strength, while the surface-decorated PHBV nanofibers and spiral configuration would significantly enhance the surface area of the NGC, promoting transport features, cellular events, and tissue regeneration. To adjust the mechanical compliance of the fiber lattice, we examined material infill densities of 25 %, 35 %, and 50 %. The TPU fiber lattice was decorated with sparsely spaced, thin layers of PHBV nanofibers, which lacked measurable mechanical strength. This composite was then rolled into a spiral NGC, providing nanofibers to facilitate intraluminal cell guidance. The fabricated micro-nanostructured spiral NGCs were characterized for surface morphology, area, composition, wettability, tensile properties, and suture retention strength. Rat Schwann cells (RSC 96) were cultured on TPU/aPHBV to evaluate their adhesion, migration, proliferation, and expression of neurogenic genes and proteins. The efficacy of TPU/aPHBV conduits in promoting axon regeneration was tested by repairing a 10 mm sciatic nerve gap for 4 months. Nerve healing outcomes were assessed based on behavioral analysis, gastrocnemius muscle weight post-innervation, histological analysis, and remyelination of regenerated nerves. This approach aims to enable effective treatment of large-gap nerve defects and restore sensorimotor functions.

2. Materials & methods

2.1. Materials

PHBV (containing 1–2 wt% hydroxyvalerate) pellets were purchased from NaturePlast, France. Chloroform ($CHCl_3$) was obtained from SRL, Mumbai. Dimethylformamide (DMF), TritonX-100 and sodium citrate were purchased from Merck, India. TPU95A filaments were purchased from Ultimaker, USA. RNA Iso Plus, Nucleospin® RNA kit, TB green, and PrimeScript™ RT Reagent Kit were procured from Takara, Japan. Dulbecco's modified Eagle's medium/F12 (DMEM/F12) and Dulbecco's phosphate buffer saline (DPBS) were procured from HiMedia, India. Penicillin/Streptomycin, Trypsin, Calcein-AM, Hoechst, and fetal bovine serum (FBS) were purchased from Thermo Fisher Scientific, India. MTS reagent was purchased from Abcam, India. Myelin basic protein (MBP) mouse monoclonal antibody and S100 calcium binding protein beta (S100 β) were purchased from Cell Signaling Technologies, Danvers, MA. Alexaflour 594™ goat anti-mouse IgG (H + L) and donkey anti-rabbit IgG (H + L) highly cross-adsorbed secondary antibody tagged with Alexafluor plus 488 antibodies were purchased from Thermo Fischer Scientific, USA. Rat Schwann cells (RSC96, passage number 8–9) were purchased from ATCC, USA. All other solvents and reagents were of analytical grade and obtained from commercial sources unless otherwise specified.

2.2. Fabrication & characterization of TPU/PHBV construct

2.2.1. Electrospinning of PHBV

PHBV pellets were dissolved in $CHCl_3$ and DMF in a ratio of 9:1, as reported previously [36]. Briefly, $CHCl_3$ was initially added to PHBV pellets and kept in a magnetic stirrer overnight at room temperature, followed by stirring in a hot water bath for about 1.5 h to dissolve the PHBV pellets completely. After letting it cool down for 10 min, DMF was added and stirred again for 1.5 h. Then, PHBV solution (12 % w/v) was loaded into a 5 mL glass syringe (Top Syringe, India) capped with a 26 G blunt needle, which was connected to a high-voltage source (HMPSKV30, Holmarc, India). Electrospinning was performed at optimized spinning parameters (applied voltage of 18 kV, a working distance of 14 cm, a flow rate of 0.01 mL/min, and for aligned fibers with the rotating drum speed of 2000 rpm). The PHBV random nanofibers (rPHBV) were deposited onto a static collector. In contrast, the aligned nanofibers (aPHBV) were deposited onto a grounded rotating drum wrapped with aluminum foil using an electrospinning instrument (HO-NFES-040, Holmarc, India).

2.2.2. 3D printing of TPU

TPU95A white filament was used to print a fiber lattice (FDM printer, Ultimaker[3] Extended, USA). A cuboid 3D model of dimension 60 x 60 × 0.4 mm (l x b x h) was designed in Tinker CAD software and exported as a 3D printable format (.stl file) (Supplementary Fig. 1). The digital.stl file was converted into G-code in Cura software and fed into the 3D printer. Table 1 shows the optimized printing parameters for the TPU fiber lattice mat. The infill density was varied to obtain TPU mats as it would affect the mechanical strength of the nerve conduit.

2.2.3. Development of TPU/PHBV constructs & spiral TPU/PHBV conduits

The 3D-printed TPU mats were stuck over the aluminum foil placed in a static/rotating collector. The PHBV nanofibers were deposited over the 3D-printed TPU mat up to a thickness of approximately 120 μm using the optimized electrospinning parameters using a static (TPU/rPHBV) or rotating drum (TPU/aPHBV) collector. The TPU/PHBV mats were rolled tightly onto a 2 mm steel rod and heat-sealed to create spiral conduits [10]. These conduits had an inner diameter of 2 mm and an outer diameter of 4 mm, matching the dimensions of rat sciatic nerves. The fabricated constructs were stored in a vacuum desiccator until further characterization.

2.2.4. Scanning electron microscope

The surface morphology of TPU, TPU/rPHBV, TPU/aPHBV mats, and their TPU/PHBV spiral conduits were imaged using a scanning electron microscope (Vega 3, TESCAN). Before imaging, the samples were sputter-coated with gold for 45 s. A 10 kV accelerating voltage was then applied for imaging [37].

2.2.5. FTIR analysis

The functional groups present in the TPU filament and PHBV fibers were examined using a Fourier Transform Infrared (FTIR) spectrometer (Spectrum 100, PerkinElmer, USA) in attenuated total reflectance (ATR) mode. The FTIR spectrum was captured between 4000 cm^{-1} and 400 cm^{-1} [38].

2.2.6. Contact angle measurement

The surface wettability of the 3D printed TPU, TPU/rPHBV, and TPU/aPHBV mats was evaluated by measuring the static water contact angle using a goniometer instrument (Rame-art, USA). Approximately 5 μL of distilled water was placed over the samples, and the contact angle was measured (n = 5) using DROP image advanced software [39].

2.3. Characterization of spiral TPU/PHBV conduits

2.3.1. Micro-CT analysis

The spiral TPU/PHBV conduits were scanned using high-resolution micro-computed tomography (Skyscan 1176, Bruker, Belgium). The sample was mounted on the holder, and the scanning was performed at an X-ray beam voltage of 45 kV, beam current of 555 μA, and 755 ms beam exposure time using no filter mode. The X-ray projected (2D) images were captured around 360° with 35 μm pixel resolution, and the 2D projections were reconstructed three-dimensionally using NRecon software. The reconstructed samples were visualized through all three planes (coronary, sagittal, and transaxial) using DataViewer software [40]. The surface area of the prepared nerve conduits was measured using CT Analyser (CTAn) software.

Table 1
Optimized parameters for fabrication of 3D printed TPU microfiber lattice.

Printing Parameters	Values
Wall thickness	0.8 mm
Wall line count	2
Top/Bottom thickness	0 mm
Printing temperature	220 °C
Build plate temperature	60 °C
Flow	100 %
Print speed	25 mm/s
Infill pattern	Grid
Layer height	0.06 mm
Infill density	25 %, 35 %, 50 %

2.3.2. Tensile strength measurements

The tensile properties of TPU/rPHBV and TPU/aPHBV spiral conduits were evaluated using a uniaxial tensile testing machine (Instron 3345, USA). The spiral conduits (n = 3) of 50 mm length and 0.4 mm outer diameter for three infill densities (25 %, 35 % & 50 %) were used for this study. The ends of the samples measuring 1 cm on top and bottom sides were clamped to the gripping units of the tensile testing machine. A load of 500 N was applied at a strain rate of 10 mm/min until the sample failure [41].

2.3.3. Suture retention strength analysis

The suture retention ability of TPU/rPHBV and TPU/aPHBV spiral conduits were measured using a uniaxial tensile testing machine (Instron 3345, USA) according to the ISO 7198:1998/2001/(R) 2004 standard. Spiral conduits of length 50 mm and inner diameter 0.4 mm were fabricated and tied using a nonabsorbable Nylon 5-0 suture (SN 3317, TRULON), leaving a 1 cm thread for clamping. The suture was clamped to the mobile gripping unit and pulled at a 10 mm/min strain rate until rupture [23].

2.4. In vitro cell culture

Rat Schwann cells (RSC 96) were cultured in DMEM/F12 media supplemented with 10 % FBS and 1 % Penicillin-streptomycin and incubated at 37 °C. The fabricated TPU/rPHBV and TPU/aPHBV constructs with different infill densities were EtO sterilized and immersed in serum-free media for 1 h before cell seeding. RSC 96 cells were seeded at a seeding density of 10,000 cells/scaffold, and the media was changed on alternative days.

2.4.1. Cell adhesion & viability

RSC 96 adhesion on TPU/rPHBV and TPU/aPHBV mats were recorded using SEM (Vega3, TESCAN) at various time points. The cell-seeded constructs (n = 4) were fixed using 3.7 % paraformaldehyde for 15 min and washed with PBS, followed by dehydration using a gradient concentration of ethanol (50 %–100 %). The dehydrated constructs were then stored in a vacuum desiccator until analysis. The viability of RSC 96 on TPU/PHBV conduits was studied using Calcein-AM staining. After 1, 3, 5, and 7 days of culture, the constructs (n = 4) were taken from the well plates and incubated with 2 μM of Calcein – AM for 30 min in dark conditions. Further, the samples were washed in DPBS and imaged at different magnifications under a confocal laser scanning microscope (FV1000, Olympus) at a laser wavelength of 499 nm [37].

2.4.2. Cell proliferation

Cell proliferation on the developed TPU/rPHBV and TPU/aPHBV mats were quantitatively determined at different time points (days 1, 3, 5, 7 & 14) using MTS assay [42]. The cellular constructs were washed with PBS and added with 50 μL of MTS reagent and 450 μL of serum-free DMEM media and incubated for 3 h at 37 °C under dark conditions. A volume of 100 μL of the incubated media was placed in a 96-well plate, and the absorbance was measured at a wavelength of 490 nm using a multi-mode plate reader (Infinite 200M, TECAN). A sample size of n = 4/group/time point and TCPS was used as a positive control.

2.4.3. Immunofluorescence staining

Maturation of Schwann cells over the TPU/aPHBV constructs was confirmed by performing immunocytochemistry for the expression of F-actin and S100β on day 7. The cell seeded constructs were fixed with 4 % paraformaldehyde for 10 min and then rinsed with PBS. The fixed cells were further permeabilized with 0.1 % Triton X-100 for 15 min at room temperature and washed with PBS. Later, the cells were incubated with 2 % bovine serum albumin (BSA) to block the unspecific binding of antibodies, followed by incubation with primary S100β antibody (1:500 dilution) overnight at 4 °C. The samples were then washed with PBS twice and incubated with donkey anti-rabbit IgG (H + L) highly cross-adsorbed secondary antibody tagged with Alexafluor plus 488 (1:1000 dilution) for 45 min at room temperature. For F-actin staining, the samples were incubated with rhodamine phalloidin (1:250 dilution) dye for 1 h and then washed with PBS twice. Further, the cell nuclei were counterstained with Hoechst in the dark for 30 s [7].

2.4.4. *Gene expression*

Schwann cells were cultured on TPU/aPHBV constructs, and gene expression profiles were studied at predetermined time points (days 1, 3, 7 & 14). The scaffolds were washed using PBS to remove dead cells, and the total RNA content (ng/mL) was isolated from cellular constructs by adding 1 mL Trizol, followed by incubation for 30 min at room temperature. Chloroform was added to the isolated RNA, centrifuged at 12,000 rpm for 15 min, and stabilized using 70 % ethanol. Purified RNA samples were obtained following the manufacturer's protocol (Nucleospin® RNA kit, Takara, Japan). cDNA conversion was done using PrimeScript™ RT Reagent Kit and the obtained cDNA was subjected to quantitative RT-PCR (Quant Studio5, Thermo Fischer, USA) to study the gene expression using TB green. The primer sequences used in this study are tabulated in Table 2 [43]. The gene expression was evaluated using the $2^{-\Delta\Delta CT}$ method and normalized with the housekeeping gene (GAPDH). Specifically, we looked at the expression of Semaphorin 3F (SEM3F), Neuropilin 2 (NRP2), Plexin 1 (PLX1), S100 calcium-binding protein beta (S100), and myelin basic protein (MBP).

2.5. *In vivo evaluation of TPU/PHBV nerve conduit*

2.5.1. *Surgical procedure*

A total of 36 skeletally mature male Wistar rats, weighing approximately 300 g, were randomly assigned to four groups – (i) control (n = 9 normal animals); (ii) sham control (n = 9 nerve exposure and closure; (iii) autograft (n = 9 reversal of the severed nerve segment), and (iv) TPU/aPHBV spiral conduit (n = 9). All animals were acclimated for one week before surgery and housed with unrestricted access to food and water in a temperature-controlled room under a 12-h light-dark cycle. All animals were maintained and cared for according to methods approved by the Institutional Animal Ethics Committee of SASTRA Deemed University (659/SASTRA/IAEC/RPP) and the Indian government animal welfare guidelines. Anesthesia was induced via intraperitoneal injection of ketamine (90 mg/kg body weight) and xylazine (7 mg/kg body weight). The dorsal region of the left leg was shaved and sterilized using 70 % ethanol. A thigh-level incision was made to expose the sciatic nerve. In the sham control group, the sciatic nerve was exposed without injury. In the autograft group, a 10 mm transected nerve segment was sutured back in reverse at both ends via the epineural sleeve technique. In the TPU/aPHBV group, the distal nerve ends were inserted into the conduit, and the epineurium was sutured to the conduit using Nylon 8-0 suture (Ethicon, USA). The surgical site was closed using absorbable Vicryl 5-0 (Ethicon, USA) and nonabsorbable Nylon 3-0 suture (Trugut, India) for muscle and skin, respectively. Post-surgery, povidone ointment was topically applied to the injury site of all animals. Animals were individually housed for 15 days to monitor behavior before being grouped into individual cages according to treatment groups.

Table 2
Forward and reverser primer sequences.

Gene	Primer	Ref
SEMA3F	Forward: GGCAGCAAGTAGGAAG Reverse: CCCAGAGGATGAAGC	[44]
NRP2	Forward: CTTGCTCCCTCTTTGCTG Reverse: TTCCTTGTGGTGTCTTCTG	
PLX1	Forward: TGAGGGGTGTGTGGATAG Reverse: CGAAGCAGGGTTAGGTTC	
GAPDH	Forward: TGGTGAAGGTCGGTGTGAAC Reverse: TTCCCATTCTCAGCCTTGAC	
S100β	Forward: ATGGTTGCCCTCATTGATGTCTTCC Reverse: ACCACTTCCTGCTCTTTGATTTCCTC	[45]
MBP	Forward: TCTGGAAAGCGAGAATTAGCATCTGAG Reverse: ACTGTCTTCTGAGGCGGTCTGAG	

2.5.2. *Elevated narrow ledged beam analysis*

Rats were trained for 5 days before surgery to adapt to the specially constructed elevated ledged and tapered beam apparatus with 165 cm length inclined at an angle of 10° with 2 cm ledges on each side. The broader end of the beam is the starting point, which narrows down the path and leads to a dark box (28 cm × 23 cm x 36 cm) filled with food pellets as a reward. The movement of the animals along the beam was recorded using a camera. The test was carried out at different experimental time points – 1st, 2nd, 3rd, and 4th month. The average foot slip ratio was calculated by measuring the total number of slips made by the left and right hind limbs and the number of hind limb steps from the video clip and was calculated using the formula [44],

$$\text{Average foot slips } (\%) = \frac{\text{Left hind limb slips} + \text{Right hind limb slips}}{\text{Total footsteps}}$$

2.5.3. *Sciatic functional index analysis*

Sciatic functional index (SFI) and toe-out angle (TOA) are two important parameters measured from the gait analysis to evaluate the sensorimotor recovery of rats. For this study, the rats were trained to walk in a confined acrylic walkway (165 cm × 15 cm) for 3 days before surgery. During measurement, the paws of the left and right hind limbs were painted with blue and green colored ink, respectively. A graph sheet was placed in the walkway, and the rats were allowed to walk on the sheet towards the dark box. The foot paw impressions were analyzed to calculate the sciatic functional index (SFI) using the formula,

$$\text{Sciatic Functional Index (SFI)} = 109.5\,\frac{(\text{ETS} - \text{NTS})}{\text{NTS}} - 38.5\,\frac{(\text{EPL} - \text{NPL})}{\text{NPL}} + 13.3\,\frac{(\text{EIT} - \text{NIT})}{\text{NIT}} - 8.8$$

PL, TS, and IT represent the print length, toe spread length, and intermediary toe spread length, respectively. PL refers to the distance from the heel to the third toe, TS refers to the distance from the first to the fifth toe, and IT refers to the distance from the second to the fourth toe. These parameters were measured for both the experimental (E) hind limb and normal (N) hind limb to determine the SFI values in each group. The SFI value of −100 indicates the complete impairment of the sciatic nerve, whereas the SFI close to 0 specifies the complete recovery of the nerve [23].

2.5.4. *Toe-out angle*

To assess the functional recovery of the sciatic nerve, the toe-out angle (TOA) of the operated leg was measured in all groups during the fourth month of the treatment period. A camera was attached to the underside of the acrylic walkway to capture images of the plantar surface of the rat's feet, and they were analyzed to determine how they spread their digits to move along the track. From the images obtained from the walking trajectory of the rat, a progression/travel line was drawn in the direction of movement of the rat, and a reference line was drawn from the calcaneus or heel region to the tip of the third digit. The angle between the progression line and the reference line was measured as TOA [46].

2.5.5. Gastrocnemius muscle index analysis

After 4 months of surgery, the rats were sacrificed to isolate the gastrocnemius muscles (which are innervated by the sciatic nerves) from both the operated and non-operated hind limbs [46]. The isolated wet muscles were weighed immediately using an electronic balance to determine the gastrocnemius muscle index (GMI) using the formula given below:

$$\text{Gastrocnemius muscle index (GMI)} = \frac{\text{Wet weight of muscle on the operated side}}{\text{Wet weight of the muscle on the non} - \text{operated side}}$$

2.5.6. Histological assessments

After the animals were sacrificed, the gastrocnemius muscles were dissected carefully and fixed in 10 % formalin solution for 1 week, followed by ethanol dehydration. The dehydrated tissues were then embedded in paraffin, sectioned into 5 μm thick sections using a microtome, deparaffinized, and rehydrated according to the protocol reported by Tao *et al.*, [47]. The cross-section of the muscles of all groups was stained using hematoxylin-eosin (H & E) to measure the diameter and area of the muscle fiber under a light microscope (Nikon, Japan). Luxol fast blue (LFB) staining was performed to visualize the myelin formation in the regenerated nerves. The sciatic nerves from the autograft and TPU/aPHBV conduit groups were retrieved and fixed in 10 % formalin for 1 week. Then, the samples were dehydrated using ethanol, followed by resin embedding (Technovit 9100 kit), and frozen until hardening. Further, the nerves were sectioned to 100 μm thickness (Secotome 60, Struer, Denmark), and then the thickness of the sections was reduced to 10 μm (Bainpol VTD polishing machine). After staining the slides with LFB dye solution, the glass slides were microscopically examined at different magnifications (Nikon, Japan) [48]. The percentage area of myelination was quantified from Luxol fast blue stained images of autografts and TPU/aPHBV nerve conduit groups using ImageJ software.

2.5.7. Immunohistochemistry studies

The longitudinal nerve sections from autograft and TPU/aPHBV conduit groups were also analyzed for the expression of myelin basic protein (MBP), confirming the myelination of Schwann cells surrounding the axons. For this experiment, the sectioned slides were immersed in xylene for 30 min to remove the resin from the tissue slices [37], followed by a microwave-assisted antigen retrieval step for 30 min at low power. Further, the tissue sections were incubated with anti-MBP primary antibody (1:250, 4 °C) overnight, followed by Alexafluor 594-tagged secondary antibody (1:500 dilution) for 30 min. Finally, the slides were stained with Hoechst for 1 min, rinsed with 1X PBS, and imaged using a confocal microscope [23].

2.6. Statistical analysis

Results are expressed as mean ± standard error of the mean (SEM), and statistical analysis was performed. Imaging experiments employed a sample size of $n = 3$, while quantitative cell culture experiments utilized a sample size $n = 4$. Mechanical testing was conducted with a sample size $n = 6$ for each group and time point. One-way analysis of variance (ANOVA) was performed for TOA and GMI analysis. Two-way ANOVA was performed for tensile strength, suture retention strength, *in vitro* experiments, number of foot slips, and SFI analysis. The values were significant at $p < 0.05$ in both cases.

3. Results

3.1. Characterization of TPU & PHBV mats

Fig. 1a–i and Supplementary Fig. 2a are SEM of aligned and random PHBV fibers used in this study. The bead-free electrospun PHBV fibers had an average diameter of 395 ± 93 nm for random fibers and 275 ± 50 nm for aligned fibers. The aPHBV fibers were aligned at an angle of approximately 94° (Fig. 1a–ii). A TPU fiber lattice in the grid pattern with different infill densities (25 %, 35 %, and 50 %) was 3D printed using optimized parameters. Fig. 1b illustrates the printed plain TPU mats, which were found to be consistent with the developed.stl file.

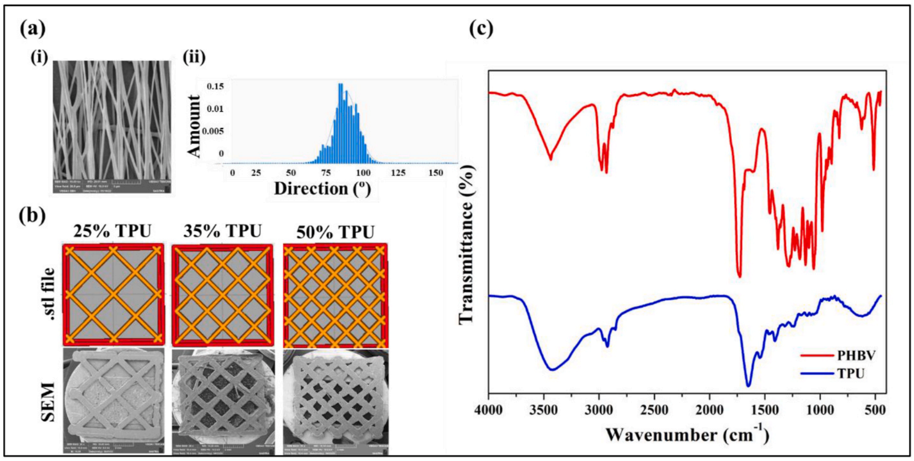

Fig. 1. PHBV nanofibers and TPU microfiber lattice were fabricated using electrospinning and 3D printing. (a–i) SEM image of aligned PHBV (aPHBV) nanofibers showing anisotropic nanofibrous features (Scale bar = 5 μm); (a-ii) Pixel intensity plot indicating aPHBV nanofibers were highly aligned at an angle of ~94°; (b) Digital (.stl) file and corresponding SEM images of 3D printed TPU mats with 25 %, 35 % & 50 % infills. The SEM images of the printed constructs exactly resemble the designed digital (.stl) file; and (c) FTIR spectra of TPU & PHBV nanofibers displayed their characteristic peaks for carbonyl, hydroxyl, and urethane bonds.

Chemical compositions of the electrospun PHBV nanofibers and pristine TPU filament were studied using ATR-FTIR spectroscopy (Fig. 1c). In the case of electrospun PHBV fibers, the stretching vibrations of the hydroxyl group were observed at 3434 cm^{-1}, and a sharp peak for C=O stretching vibration of the ester bonds was identified at 1725 cm^{-1}. Peaks at 2974 cm^{-1} and 2931 cm^{-1} represent the asymmetric and symmetric stretch of CH2 groups, respectively, whereas peaks at 1451 cm^{-1} and 1379 cm^{-1} correspond to the asymmetric and symmetric stretch of CH3 groups. The C-O-C stretching vibrations of PHBV fibers appear at 1290 cm^{-1} and 1045 cm^{-1}, respectively, while a peak at 979 cm^{-1} represents the C-C stretching of PHBV [46]. The FTIR bands of the extruded thermoplastic polyurethane filament exhibited all the characteristic peaks as reported in previous studies [49]. Peaks at 3436 cm^{-1}, 1546 cm^{-1}, and 1743 cm^{-1} correspond to N-H stretching, N-H deformation, and C=O stretching of the urethane bond structure, respectively. In addition, peaks at 2924 cm^{-1} and 2853 cm^{-1} represent the symmetric and asymmetric vibrational stretch of CH bonds in TPU.

3.2. *Morphology of TPU/PHBV constructs*

The spiral micro-nano structured NGC morphology demonstrates fabrication feasibility for both larger (Fig. 2d human) and smaller (Fig. 2f rat) sizes. Supplementary Figs. 2a and 2b shows the aligned and random PHBV nanofibers deposited over the 3D-printed TPU constructs of different infill densities (25 %, 35 %, and 50 %). The fibers were cut to the desired dimensions for further characterization experiments. Fig. 2b illustrates the surface morphology of the electrospun random and aligned PHBV on 3D-printed TPU. TPU/aPHBV constructs (where aPHBV fibers are present on top of the 3D-printed TPU mats) were wrapped around a 2 mm metal rod and heat-sealed to obtain a spiral conduit with a 4 mm inner diameter (Fig. 2c). SEM images of the spiral 35 % TPU/PHBV human sized conduits revealed the concentric arrangement of the printed TPU and electrospun PHBV nanofibrous matrices (Fig. 2d). The contact angles for plain TPU, TPU/rPHBV, and TPU/aPHBV constructs were measured as 75.27 ± 3.06°, 103.07 ± 5.43°, and 113.20 ± 2.98°, respectively (Fig. 2e). Fig. 2f shows the micro-CT images of TPU/PHBV smaller rat sciatic nerve sized conduits where TPU of different infill densities (25 %, 35 %, and 50 %) and PHBV fibers were arranged in a concentric pattern (spiral). Both 35 % TPU/PHBV and 50 % TPU/PHBV nerve conduits had minimal sharp edges at their periphery compared to 25 % TPU/PHBV conduits.

3.3. *Mechanical properties of TPU/PHBV conduits*

The ultimate tensile strength, load at break, and Young's modulus of plain TPU, spiral TPU/rPHBV, and TPU/aPHBV conduits with 25 %, 35 %, and 50 % infill densities were evaluated (Fig. 3a–c). As infill densities of TPU in TPU/PHBV conduits increased, mechanical properties also improved. TPU/rPHBV spiral conduits demonstrated higher ultimate tensile strength and load at break values compared to TPU/aPHBV spiral

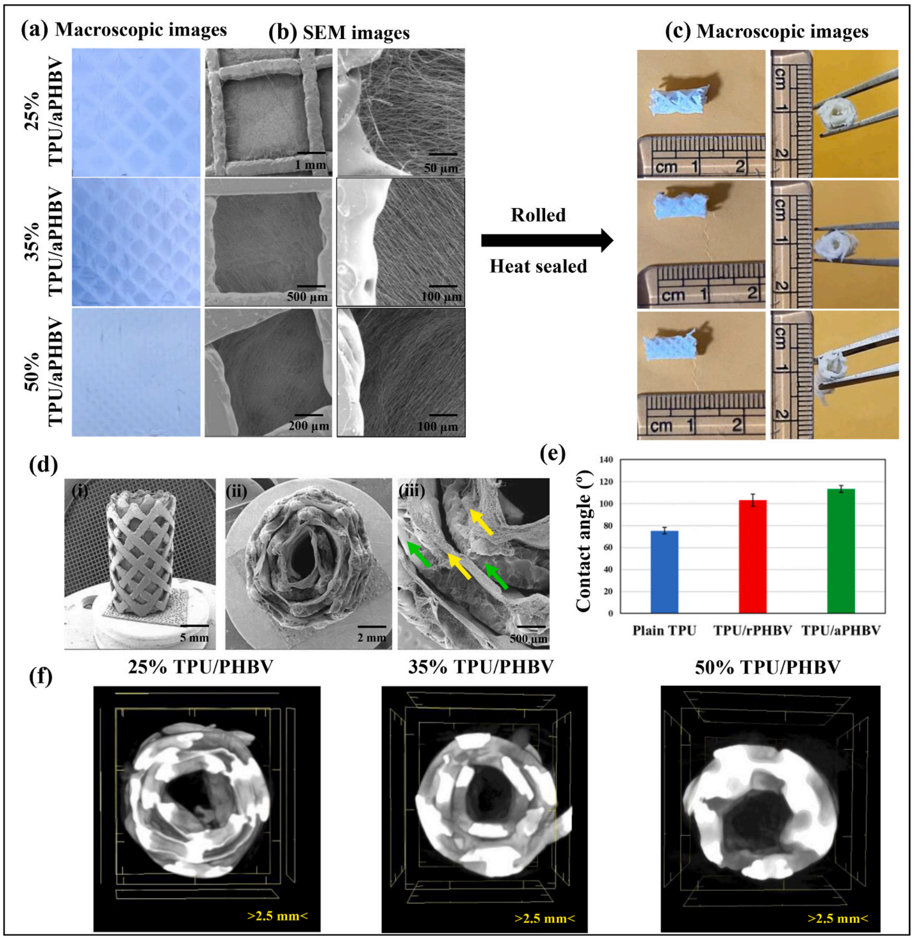

Fig. 2. The spiral micro-nano structured NGC morphology demonstrates fabrication feasibility for both larger (human) and smaller (rat) sizes. (a & b) Optical and SEM images present examples of aligned PHBV nanofibers on the TPU microfiber lattice. **(c)** A 2 mm × 10 mm spiral NGC example was produced by rolling and heat sealing the edges. **(d)** Larger NGC examples, applicable to human nerves, are shown. The green arrow indicates TPU microfibers, and the yellow arrow points to PHBV nanofibers in the spiral NGC. **(e)** Water contact angle measurements indicate improved hydrophilicity for rPHBV/aPHBV compared to TPU. **(f)** Micro-CT images of smaller NGCs used for rat sciatic nerve reconstruction are presented.

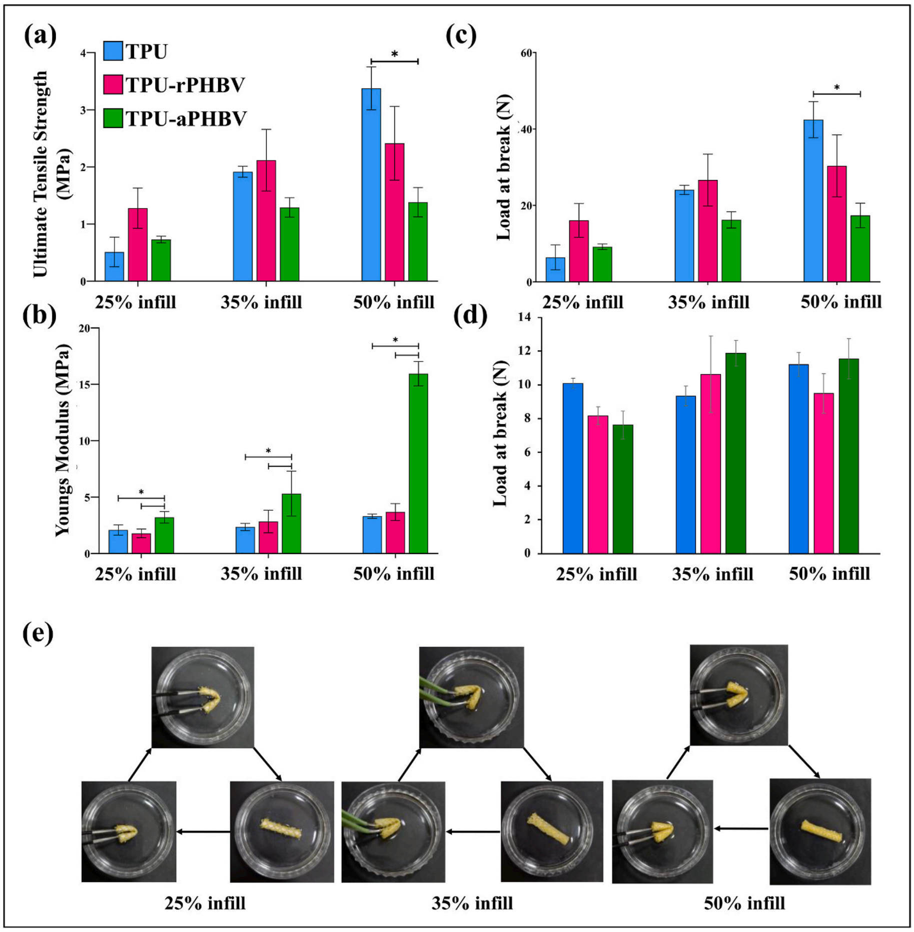

Fig. 3. The increased TPU infill density from 25 % to 50 % significantly enhanced the tensile properties of the spiral NGC. Improvements were observed in (a) Ultimate tensile strength, (b) Young's modulus, (c) Load at break, & (d) Suture retention strength (*p < 0.05) and (e) NGCs with different infill densities are kink resistant.

conduits, although the differences were not statistically significant. However, the ultimate tensile strength and load at break of 25 % and 35 % infills for all three spiral conduits (TPU, TPU/rPHBV, & TPU/aPHBV) were comparable, with no significant differences. For plain TPU with 50 % infill, Young's modulus values were significantly higher than those of other 50 % infill density groups (TPU/rPHBV & TPU/aPHBV). As shown in Fig. 3c, TPU/aPHBV conduits of all infills (25 % TPU/aPHBV: 3.20 ± 0.22 MPa; 35 % TPU/aPHBV: 4.73 ± 0.73 MPa; 50 % TPU/aPHBV: 10.11 ± 0.24 MPa) exhibited significantly higher Young's modulus compared to plain TPU (25 % TPU: 2.08 ± 0.20 MPa; 35 % TPU: 2.35 ± 0.14 MPa; 50 % TPU: 3.30 ± 0.08 MPa) and TPU/rPHBV (25 % TPU/rPHBV: 1.77 ± 0.17 MPa; 35 % TPU/rPHBV: 2.83 ± 0.44 MPa; 50 % TPU/rPHBV: 4.84 ± 0.75 MPa) conduits. Plain TPU conduits demonstrated significantly lower Young's modulus than TPU/rPHBV conduits of different infills. Fig. 3d indicates that there were no statistically significant differences in suture retention strength among plain TPU, TPU/rPHBV, and TPU/aPHBV conduits printed with different infill densities. These NGCs with different infill densities of TPU were also kink-resistant under wet conditions (Fig. 3e).

3.4. *In vitro assessments*

3.4.1. *Schwann cell adhesion & viability*

Adhesion of RSC-96 cells on TPU/rPHBV and TPU/aPHBV constructs was qualitatively assessed using scanning electron microscopy. The images revealed that the cells were well-attached to both aligned and random PHBV fibers (Fig. 4a & Supplementary Fig. 3a). Within 5 days of culture, the cells covered the entire constructs. Calcein AM staining of RSC 96 cells cultured on TPU/rPHBV (Supplementary Fig. 3b) and TPU/aPHBV (Fig. 4b) constructs demonstrated cell viability up to day 7 and a widespread distribution throughout the constructs. From day 5, these cells exhibited spindle-shaped and elongated cytoplasmic extensions, characteristic of native RSC 96 cells. In TPU/aPHBV constructs with various TPU infills, these extensions were oriented along the direction of aligned PHBV fibers (Supplementary Fig. 4 and 4c). In contrast, cells on TPU/rPHBV constructs grew randomly on the surface.

3.4.2. *Schwann cell proliferation & surface marker expression*

Fig. 4d and Supplementary Fig. 3c confirm higher Schwann cell proliferation on both TPU/rPHBV and TPU/aPHBV constructs compared to TCPS controls up to 14 days. While no significant differences were observed between TPU/rPHBV and TPU/aPHBV constructs of all three infills at each time point, cell proliferation on TCPS plateaued from day 5 onwards and was significantly reduced compared to TPU/aPHBV constructs on day 14. Fig. 4e demonstrates that RSC 96 cells on TPU/aPHBV constructs expressed S100 on day 7, confirming that these constructs did not adversely affect the native cell surface marker expression of the cultured RSC 96 cells.

3.5. *Gene expression analysis*

Schwann cell-specific gene expression profiles for semaphorin 3F (SEMA3F), plexin 1 (PLX1), neuropilin 2 (NRP2), S100 calcium-binding protein beta (S100β), and myelin basic protein (MBP) were studied on

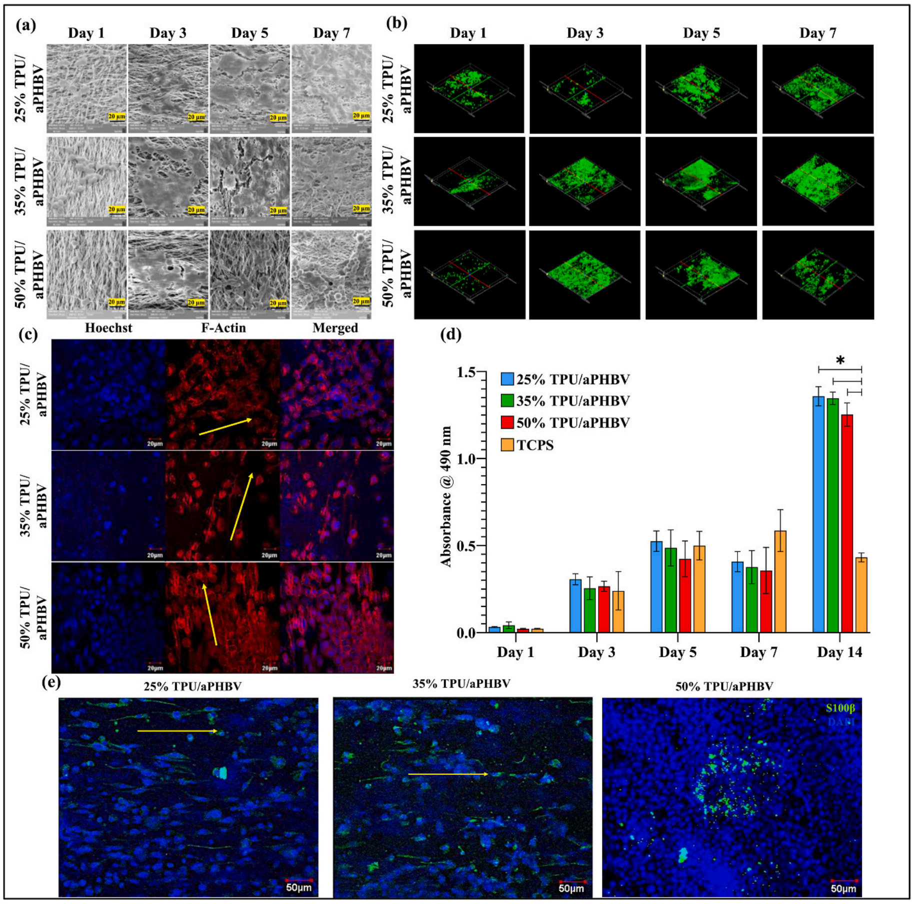

Fig. 4. All infill densities supported Schwann cell adhesion and progressive growth over time, along with specific S100β expression. (a) SEM images show Schwann cell attachment and growth over time; **(b & c)** Confocal images of Calcein AM-stained cells at different time points; **(c)** F-actin staining of Schwann cells cultured over TPU/aPHBV constructs on day 7, depicting cell orientation along the fiber direction (yellow arrows); **(d)** MTS assay results show progressive cell growth, consistent with the qualitative observations from **(a)** and **(b)** (*p < 0.05); **(e)** Neuron-specific S100β marker expression on day 7 demonstrates alignment along the fiber direction (yellow arrow).

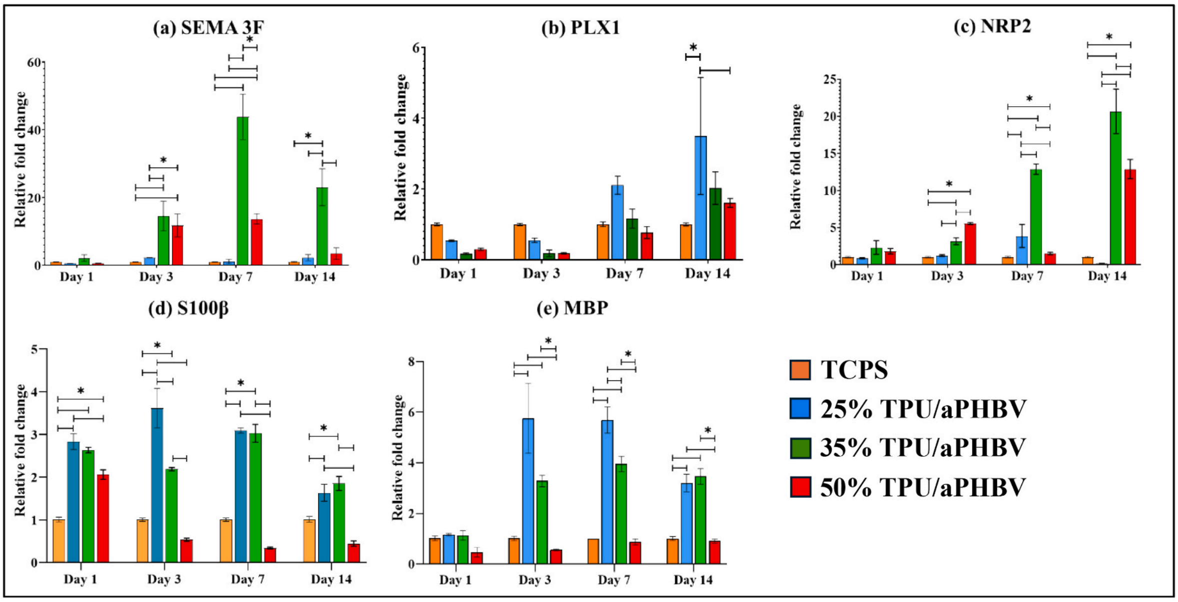

Fig. 5. S100β and MBP gene expression by Schwann cells was significantly elevated on NGCs with 25 % and 35 % infill densities. Relative fold changes compared to the β-Actin housekeeping gene were observed for **(a)** SEMA3F, **(b)** NRP2, **(c)** PLX1, **(d)** S100β, and **(e)** MBP over a 14-day period (*p < 0.05).

TPU/aPHBV conduits up to 14 days. Fig. 5 demonstrates that gene expression was higher at later culture periods (days 7 & 14) in all experimental groups compared to TCPS. Particularly, a gradual increase in the expression of these genes was observed in the 35 % TPU/aPHBV constructs until day 7. Significant upregulation of SEMA3F (~40 fold), NRP2 (~20 fold), PLX1 (~2 fold), S100β (~3 fold), and MBP (~6 fold) was evident in the 35 % TPU/aPHBV constructs compared to other groups (25 % TPU/aPHBV & 50 % TPU/aPHBV). Interestingly, in 35 % TPU/PHBV constructs, we observed a significant downregulation of genes on day 14 compared to day 7. However, there was a noticeable increase in the expression of PLX1 (~4 fold) in 25 % TPU/aPHBV constructs and NRP2 (~35 fold) in 50 % TPU/aPHBV constructs on day 14 compared to other groups.

3.6. *In vivo evaluation*

A 10 mm critical-sized sciatic nerve defect was created in Wistar rats to evaluate the regenerative potential of the 3D-printed TPU/aPHBV conduits. The study compared the TPU/aPHBV group with normal, sham control, and autograft groups. All animals tolerated anesthesia well, recovered from surgery, and survived for four months. Post-surgery, the animals experienced mild difficulty in walking, which resolved within 7 days. There was no surgical inflammation or infection at the surgery site. Importantly, all animals remained active and exhibited normal behavior throughout the study, indicating the absence of adverse effects.

3.6.1. *Functional recovery and gait measurements*

Quantitative measurements of hindlimb motor and sensory function recovery were performed using a skilled locomotor test (elevated narrow-ledged beam test) and walking track analysis. Fig. 6a shows the percentage of foot slips/errors made by animals at different time points in each group, providing data to assess motor balance and recovery. During the initial time points (months 1 and 2), both the autograft and TPU/aPHBV conduit groups exhibited increased foot slips compared to control and sham control animals. However, this number gradually decreased in later time points (months 3 & 4), indicating gradual but significant recovery. After 4 months, the number of foot slips in the autograft and TPU/aPHBV-implanted animals was comparable, with no significant differences. From the walking track study, parameters such as sciatic functional index (SFI) and toe-out angle were measured. Control and sham control animals maintained SFI values close to 0 throughout the study period, indicating no sciatic nerve damage. In contrast, autograft and TPU/aPHBV conduit group animals initially showed significantly lower SFI values (−83.61 ± 1.34 and −90.88 ± 1.8, respectively) during the first month, reflecting hindlimb impairment due to the sciatic nerve defect. SFI values progressively decreased in both treated groups (autografts and TPU/aPHBV conduit group) over the study period (Fig. 6b). After 4 months, SFI values in the autograft and TPU/aPHBV groups were calculated to be −58.90 ± 5.53 and −60.73 ± 0.59, respectively, which were statistically different from values at earlier time points (months 1, 2, & 3). Notably, the SFI of the conduit-implanted group was like that of the autograft group. Digital images of the foot imprints and operated hindlimb depicted toe-spreading with no contracture formation (Fig. 6c). Fig. 6d shows the toe-out angle (TOA) measured in the operated hindlimb of all animals after four months. TOA values in the autograft and TPU/aPHBV conduit-implanted groups were significantly different from those of normal and sham control animals.

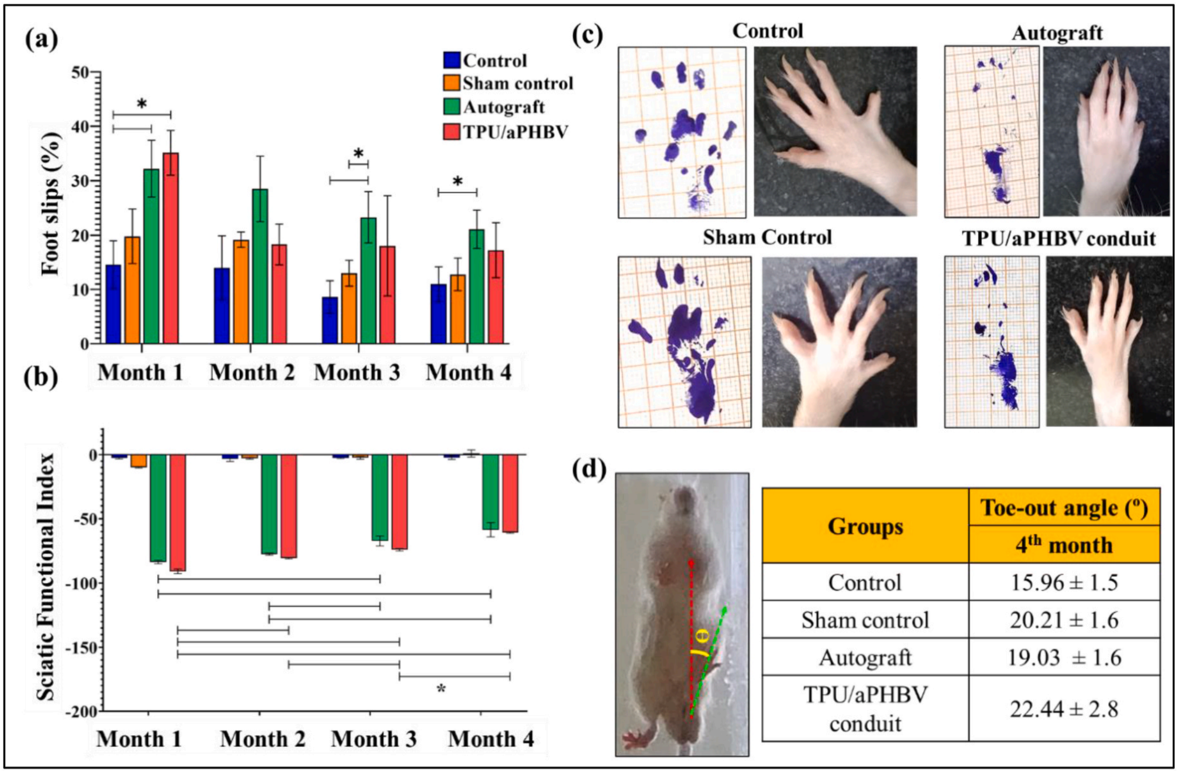

Groups	Toe-out angle (°)
	4th month
Control	15.96 ± 1.5
Sham control	20.21 ± 1.6
Autograft	19.03 ± 1.6
TPU/aPHBV conduit	22.44 ± 2.8

Fig. 6. Spiral TPU/aPHBV NGCs with 35 % infill density demonstrated comparable foot slip rates and SFI to autografts in a 1-cm sciatic nerve injury defect at 4 months post-surgery. Behavioral assessments were conducted to evaluate nerve function recovery over 4 months. **(a)** Foot fault/slip rates of the operated hindlimb were measured using an elevated ledge beam apparatus. **(b)** The sciatic functional index (SFI) was assessed using the walking track test. **(c)** Representative photographs of foot imprints and the operated hindlimb showcasing toe-spreading at 4 months. **(d)** Toe-out angle (TOA) analysis of the operated hindlimb in various animals at 4 months. The TOA was calculated as the angle between the red progression line and the green reference line drawn on the rat during walking track analysis (* denotes $p < 0.05$).

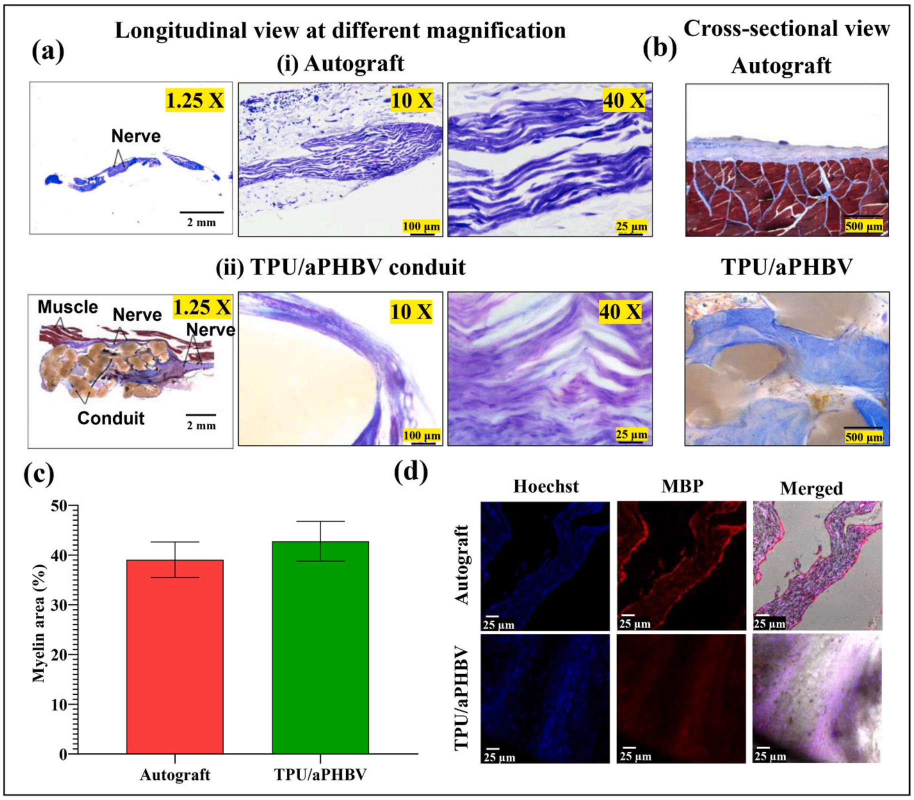

Fig. 7. Spiral TPU/aPHBV NGCs with 35 % infill density demonstrated myelin sheath formation and myelinated area comparable to autografts at 4 months. (a) Histological analysis using Luxol fast blue staining revealed myelin sheaths around regenerated axons in both autograft **(a-(i))** and spiral **(a-(ii))** TPU/aPHBV NGC groups at various magnifications. Cross-sectional views **(b)** further confirmed myelin sheath formation. **(c)** Quantitative analysis showed comparable percentages of myelinated area and MBP expression **(d)** between the two groups, suggesting effective nerve regeneration with the spiral TPU/aPHBV NGCs.

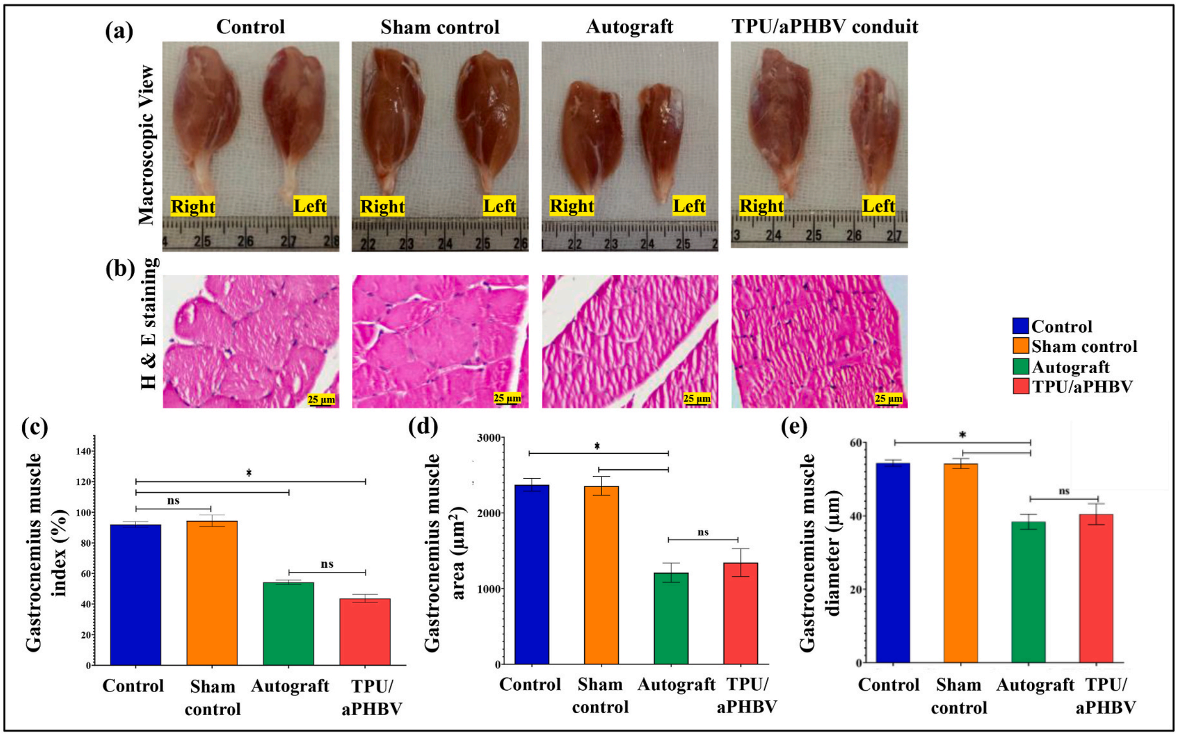

Fig. 8. Spiral TPU/aPHBV conduits and autografts demonstrated comparable gastrocnemius muscle weight and morphology 4 months post-surgery. (a) Representative images of gastrocnemius muscles in the operated and contralateral limbs. **(b)** H&E staining of gastrocnemius muscle cross-sections (40× magnification, scale bar: 25 μm). **(c)** Wet weight ratio of gastrocnemius muscles. **(d&e)** Gastrocnemius muscle area and diameter measurements obtained from H&E-stained images using Nikon software (ns denotes non-significant, * denotes $p < 0.05$).

3.6.2. Luxol fast blue (LFB) & immunohistochemical staining

Myelin sheath formation and distribution in the regenerated axons of TPU/aPHBV nerve conduits and autograft groups were evaluated using LFB staining, which selectively stains the phospholipids of the myelin sheath. Fig. 7a and b shows the light microscopic images of LFB-stained autograft and TPU/aPHBV conduit nerves after 4 months. Both longitudinal (Fig. 7a) and cross-sectional (Fig. 7b) views of autografts and TPU/aPHBV conduit groups demonstrated enhanced myelin sheath formation along the entire defect area. The cross-sectional images of TPU/aPHBV conduits also confirmed the regeneration of myelinated axons in the middle regions. Additionally, TPU/aPHBV conduits exhibited a similar percentage of myelinated area compared to autografts (Fig. 7c). Further evidence of myelination potential was obtained from longitudinal nerve sections of TPU/aPHBV conduit and autograft groups using anti-MBP staining, which revealed positive expression of myelin proteins in the conduit groups, like autografts (Fig. 7d).

3.6.3. Gastrocnemius muscle analysis

The gastrocnemius muscle was isolated from both the operated and non-operated hindlimbs of all groups. Gastrocnemius muscles from the operated limbs exhibited size reduction compared to those from the non-operated hindlimbs in the treatment groups (Fig. 8a) and were stained with H&E (Fig. 8b). The wet weight of the gastrocnemius muscle was measured to calculate the gastrocnemius muscle index (GMI). The GMIs for the control, sham control, autograft, and TPU/aPHBV implanted groups were 92.04 ± 1.88, 94.46 ± 3.73, 54.22 ± 1.49, and 43.67 ± 2.66, respectively (Fig. 8c). While muscle weight gain recovery was low in both the autograft and TPU/aPHBV conduit groups compared to the control and sham control groups, there was no significant difference between the autograft and TPU/aPHBV groups. H&E staining of gastrocnemius muscles isolated from the operated hindlimbs of the treatment groups revealed similar muscle fiber area and diameter at 4 months postoperatively, with no statistical differences (Fig. 8d & e).

4. Discussion

In this study, we developed a biomimetic TPU/PHBV nerve guidance conduit that incorporates nanoscale ECM-mimic structures and microscale features through the integration of 3D printing and electrospinning. We hypothesized that this hybrid TPU/aPHBV peripheral nerve conduit would enhance nerve regeneration, facilitate axon directionality and signal transmission, and ultimately lead to the innervation of the gastrocnemius muscle. The electrospun aPHBV nanofibrous matrices provided an intraluminal cue for axonal guidance while allowing for practical diffusion. The outer 3D-printed TPU meshes offered sufficient mechanical strength and flexibility to withstand ambulatory forces. Moreover, TPU and PHBV are FDA-approved, biocompatible, and biodegradable polymers, making them ideal candidates for large-gap nerve regeneration applications [50,51].

TPU meshes/mats were 3D printed with three infill densities (25 %, 35 %, and 50 %) using the FDM technique. PHBV nanofibers were electrospun in random (rPHBV) and aligned (aPHBV) orientations onto these TPU mats, resulting in TPU/rPHBV and TPU/aPHBV constructs. PHBV nanofibers were successfully deposited on the 3D-printed TPU mats and exhibited a high degree of alignment on TPU/aPHBV constructs with 35 % and 50 % infills compared to 25 % infill constructs. This may be attributed to greater physical contact between the PHBV fibers and the 3D-printed TPU mats at higher infill densities. FTIR analysis confirmed the presence of characteristic peaks for PHBV and TPU. Contact angle measurements revealed that PHBV polymer is hydrophobic, consistent with previous findings [47]. The hybrid TPU/rPHBV and TPU/aPHBV constructs were more hydrophobic than the 3D-printed plain TPU mat (100 % infill density). This increased hydrophobicity may be due to the entrapment of atmospheric air within the porous PHBV fibers, which reduces their interaction with water [48]. Additionally, the TPU/aPHBV construct exhibited a higher contact angle than the TPU/rPHBV constructs. This may be attributed to a decreased number of pores and reduced pore size in aligned nanofibers [39]. Although aligned nanofibers may have a higher contact angle, they are believed to provide a favorable microenvironment for neural outgrowth and alignment, mimicking Bands of Büngner during nerve regeneration [52–54].

Assessing mechanical properties is crucial for nerve guidance conduits (NGCs) as they must maintain axon and Schwann cell integrity while preventing mechanical shocks to endoneurium structures. Ideal NGCs should possess mechanical properties like nerve tissue [55]. From our previous work, PHBV matrices exhibited a tensile modulus of 1028 ± 201 MPa and a tensile strength of 1.40 ± 0.23 MPa [37]. The TPU/rPHBV and TPU/aPHBV constructs were fabricated with varying infill densities (25 %, 35 %, and 50 %) and spiraled over a metal rod. TPU/aPHBV conduits were designed with PHBV fibers oriented longitudinally to mimic the native nerve ECM microenvironment, while TPU/rPHBV conduits had randomly oriented PHBV fibers. The ultimate tensile strength of 35 % TPU/PHBV conduits (35 % TPU/rPHBV: 2.12 ± 0.54 MPa; TPU/aPHBV: 1.28 ± 0.17 MPa) was comparable to acellular human nerve grafts (1.4 ± 0.29 MPa). Conduits with 25 % and 35 % infills exhibited Young's modulus values (25 % TPU/aPHBV: 3.44 ± 0.02; 35 % TPU/aPHBV: 6.07 ± 0.59; 25 % TPU/rPHBV: 1.78 ± 0.17 MPa; 35 % TPU/rPHBV: 2.83 ± 0.45 MPa) like commercially available PGA-based nerve conduits (Neurotube®: 4 ± 2 MPa). In contrast, the 50 % TPU/PHBV nerve conduit, with both random and aligned PHBV fibers, demonstrated higher mechanical strength and stiffness than other TPU/PHBV conduits. This suggests that such conduits may not be ideal for nerve tissue regeneration. The 3D-printed plain TPU mats significantly contributed to the mechanical properties of the TPU/PHBV nerve conduits. Plain TPU spiral conduits exhibited higher mechanical strength values than PHBV-deposited TPU conduits, supporting our hypothesis. Additionally, random and aligned PHBV fiber-deposited TPU conduits showed no significant differences in mechanical properties. While an ideal mechanical property for nerve scaffolds has not been definitively identified, excessively stiff scaffolds may not accurately mimic the native nerve ECM mechanical properties. Peripheral nerves are relatively fragile and soft tissues, and highly rigid scaffolds may not be optimal for nerve conduit development [56]. The retention of mechanical strength and the formation of biocompatible degradation products are essential for supporting large-gap nerve defects. Our previous work extensively characterized PHBV- and TPU-based nerve guidance conduits (NGCs) for degradation [23,37].The degradation profiles of commercially available PCL-based conduits like Neurotube® and Neurolac® align with those presented in this manuscript [57,58]. The current study used less TPU material than commercial tubular conduits to promote degradation through an optimized structural design.

The suture retention strength of TPU/rPHBV and TPU/aPHBV conduits was sufficient for all three infill densities, consistent with previous reports [59]. Micro-CT images revealed that 25 % TPU/PHBV spiral conduits exhibited marked roughness at both ends due to reduced infill density. This could potentially damage surrounding tissues during or after implantation (Fig. 2f). In contrast, higher infill densities (35 % and 50 %) resulted in more tightly spiraled conduits with smoother curvatures. Based on these mechanical assessments, both 25 % TPU/PHBV and 35 % TPU/PHBV hybrid conduits demonstrated mechanical properties comparable to native peripheral nerves, making them potentially suitable for clinical implantation. While the 35 % and 50 % TPU/PHBV nerve constructs were also suitable for implantation, the 35 % TPU/PHBV option may offer advantages in terms of mechanical properties and reduced tissue damage.

Schwann cells are essential for peripheral nerve regeneration. When peripheral nerve damage occurs, Schwann cells and fibroblasts are recruited to the injury site within a week. During Wallerian degeneration, Schwann cells play crucial roles in axonal debris removal, formation of Bands of Büngner, stimulation of growth factors, and remyelination [60]. *In vitro*, RSC 96 cells cultured on TPU/rPHBV and TPU/aPHBV constructs demonstrated strong adhesion and *alignment* along the PHBV fiber direction (Fig. 4a). Calcein AM staining and MTS assay results confirmed the cytocompatibility of the TPU and PHBV materials (Fig. 4b & Supplementary Fig. 4). The aligned PHBV fibers in TPU/PHBV constructs acted as a potent path-finding cue, guiding cell orientation and promoting synaptic connection formation. This aligns with previous findings by Ref. [61], who fabricated 3D dual-scale scaffolds with electrospun PCL fibers on 3D-printed PCL scaffolds. The perpendicular arrangement of these fibers provided anisotropic mechanical properties and facilitated Schwann cell elongation, guidance, and alignment. While both TPU/rPHBV and TPU/aPHBV constructs exhibited mechanical stability suitable for nerve regeneration, Schwann cells migrated and aligned more effectively in TPU/aPHBV constructs, consistent with previous reports [62]. Additionally, the TPU/PHBV spiral conduits had a significantly larger surface area (25 % TPU/PHBV: 698.97 mm^2, 35 % TPU/PHBV: 500.06 mm^2, 50 % TPU/PHBV: 327.61 mm^2) compared to commercially available nerve conduits (e.g., NeurolacTM: 205.26 mm^2). The increased surface area in TPU/PHBV conduits likely contributed to enhanced Schwann cell proliferation and accelerated nerve regeneration *in vivo*.

Expression of developmental genes like SEMA3F, NRP2, and PLX1 was analyzed using RT-PCR. SEMA3F, a soluble extracellular protein involved in axonal guidance and development, dimerizes with NRP2 (a cell surface glycoprotein) via sulfide linkages. This complex then binds to PLX1, a co-receptor, activating intracellular signal transduction pathways that support cell survival and proliferation [63]. MBP is an extrinsic membrane protein, highly expressed in myelinated peripheral nerves whereas S100β aids in promoting neurite extension, leading to enhanced cell survival [45]. Nune *et al.*, investigated the efficacy of RADA-16 modified PLGA electrospun nerve guidance conduits for treating critical-sized sciatic nerve injury. The biofunctional conduits, with self-assembled RADA-16 peptides, demonstrated good cytocompatibility and enhanced expression of native surface marker proteins (neurofilament & S100β) and growth-specific genes *in vitro*. RT-PCR analysis revealed upregulation of SEMA3F and NRP2 at earlier time points (days 3 & 7), followed by downregulation at later time points (day 14) [44]. The initial upregulation of SEMA3F and NRP2 likely created a favorable environment for Schwann cell formation of Bands of Bungner. However, their subsequent downregulation may be attributed to the predominant formation of myelin sheaths over aligned Schwann cells [44]. The increased expression of these genes in TPU/aPHBV constructs compared to TCPS controls suggests that the topographical cues provided by PHBV nanofibers facilitated Schwann cell alignment and growth. Among the different TPU/aPHBV constructs, the 35 % TPU/aPHBV construct demonstrated significantly increased gene expression until day 7, possibly due to its mechanical properties resembling native peripheral nerves. Further biomechanical studies on Schwann cell proliferation and alignment on TPU/aPHBV constructs would be beneficial to elucidate the superior performance of the 35 % TPU/aPHBV construct compared to other infill densities. Based on tensile properties, *in vitro* cytocompatibility, and ease of fabrication, the 35 % TPU/aPHBV conduit was selected for *in vivo* implantation.

The *in vivo* efficacy of TPU/aPHBV conduits was evaluated in a 10-mm critical-sized sciatic nerve injury model in Wistar rats over 4 months. The Wistar rats used in this study were smaller, and the sciatic nerve measured about 1.5–1.8 cm before splitting into the tibial and common peroneal (fibular) nerves. Due to anatomical constraints, we could only create a 1 cm-long defect, which is still significantly large. Sensorimotor recovery was assessed using the elevated narrow ledge beam test and walking track analysis. Common challenges encountered during the experiments included self-mutilation of the conduit-implanted toes, flexion contracture, and imprint smearing/tail dragging during walking track analysis, consistent with previous reports [13]. Animals exhibiting self-mutilation or imprint smearing were excluded from the analysis. Immediately post-surgery, the operated toes in the hindlimb demonstrated significant improvements in paw slips, toe-out angle, and SFI values, comparable to autografts. This suggests that the PHBV nanofibrous morphology effectively facilitates directed sciatic nerve regrowth and functional recovery. Previous studies have also investigated the use of various biomaterials for sciatic nerve repair. Tagandurdyyeva et al. [64] developed a PLA conduit filled with chitosan nanofibrils and observed improved SFI values in rats with a 10-mm sciatic nerve defect compared to autografts. Biazar et al. [65] fabricated electrospun PHBV conduits for a 30-mm sciatic nerve defect and reported significant improvements in motor function, including toe-out angle and toe spread, after 16 weeks. Myelin sheath formation is crucial for regulated axonal transport and signal transmission [66]. Histological analysis of the sciatic nerves in TPU/aPHBV-implanted animals revealed blue staining and increased MBP expression, indicating myelin formation in the regenerated nerves. Quantification of the myelinated area demonstrated comparable levels to autografts. Manoukian et al. also observed remyelination in autografts and chitosan-based NGCs, although the rate was not statistically significant [67].

In addition to innervating the gastrocnemius, tibial, and plantar muscles of the rat's hindlimb, the sciatic nerve plays a crucial role in their function. Following sciatic nerve damage, gastrocnemius muscles often exhibit atrophy, characterized by reduced weight, muscle fiber area, and diameter. To assess functional recovery, we measured the wet weight and morphology of these muscles. The TPU/aPHBV group demonstrated significant recovery of gastrocnemius muscle wet weight, quantity, and shape (as analyzed by H&E staining, Fig. 8b), comparable to autograft animals. This suggests that the TPU/aPHBV conduit effectively supports sciatic nerve regeneration. Previous studies have also shown promising results for 3D-printed nerve conduits in promoting muscle recovery after nerve injury. For instance, Wu *et al.*, [68] developed a 7,8-DHF-loaded GelMA/SF-MA hydrogel conduit and observed comparable gastrocnemius muscle wet weight and diameter in conduit-implanted rats compared to autografts. Similarly, Xue *et al.*, [69] fabricated a TEN graft using silk fibroin/chitosan loaded with SKP-induced Schwann cells and achieved similar gastrocnemius muscle wet weight and cross-sectional area in TEN-implanted animals compared to autografts. These findings highlight the importance of supporting cell-based therapies and bioactive cues in nerve regeneration. In conclusion, the *in vivo* efficacy of the TPU/aPHBV conduit, as demonstrated by functional tests, morphometric measurements, and histological analysis, is comparable to that of autologous nerve grafts. This suggests that the PHBV nanofibers and TPU matrix effectively support nerve regeneration and provide sufficient mechanical strength under physiological conditions. A limitation of this study is the lack of electrophysiological studies to assess compound action muscle potentials (CMAPs). CMAPs are essential for validating the conduit's impact on nerve conduction ability in the regenerated nerves. Therefore, future research should include comprehensive *in vitro* and *in vivo* studies on larger animals with longer sciatic nerve injuries (>4 cm) using the developed spiral TPU/aPHBV nerve conduits.

5. Conclusions

A spiral TPU/PHBV micro-nano structured nerve guidance conduit was developed using 3D printing and electrospinning techniques. The microstructure was a 3D-printed fiber lattice with 25 %, 35 %, and 50 % infill density and decorated with aPHBV and rPHBV electrospun nanofibers. The surface area of the fabricated TPU/PHBV spiral conduits was significantly higher (25 % TPU/PHBV: 698.97 mm^2, 35 % TPU/PHBV: 500.06 mm^2, 50 % TPU/PHBV: 327.61 mm^2) compared to commercially available nerve conduits like Neurolac™ (205.26 mm^2). This highlights the advantage of the spiral structure in providing a greater surface area for cellular interaction. The TPU/aPHBV nerve constructs with 25 % and 35 % infills of TPU exhibited good tensile strength and suture ability, which were equivalent to commercially available nerve guides (e.g., Neurotube®) and peripheral nerve tissues with additional advantages such as surface area and nanotopographical cues to enhance nerve regeneration. *In vitro* experiments revealed that aligned PHBV nanofibers on the TPU/aPHBV constructs had enhanced Schwann cell viability, attachment, and migration in aligned pattern with the expression of S100 marker and nerve growth-specific genes, confirming cytocompatibility of TPU and PHBV nanofibers. Further, implantation of the developed acellular TPU/aPHBV nerve conduits in a 10 mm sciatic nerve defect rat model for 4 months restored the normal sensory and motor functions of sciatic nerves with remyelination and recovery of sensory-motor functions analogous to autologous nerve grafts. Hence, these results proved that the fabricated TPU/aPHBV spiral nerve conduits would be a promising alternative for autografts to promote nerve regeneration in long-distance and large-diameter nerve gaps.

CRediT authorship contribution statement

Allen Zennifer: Data curation, Formal analysis, Methodology, Writing – review & editing. **S.K. Praveenn Kumar:** Methodology. **Shambhavi Bagewadi:** Methodology. **Swathi Unnamalai:** Methodology. **Davidraj Chellappan:** Methodology. **Sama Abdulmalik:** Methodology. **Xiaojun Yu:** Formal analysis, Methodology. **Swaminathan Sethuraman:** Formal analysis, Funding acquisition, Methodology, Writing – review & editing. **Dhakshinamoorthy Sundaramurthi:** Data curation, Formal analysis, Funding acquisition, Methodology, Project administration, Supervision, Writing – review & editing. **Sangamesh G. Kumbar:** Conceptualization, Data curation, Formal analysis, Methodology, Project administration, Supervision, Writing – review & editing.

Ethics Approval and consent to participate

All animals were maintained and cared for according to methods approved by the Institutional Animal Ethics Committee of SASTRA Deemed University (659/SASTRA/IAEC/RPP) and the Indian government animal welfare guidelines.

Declaration of competing interest

Corresponding author Sangamesh G. Kumbar is an Associate Editor for Bioactive Materials and was not involved in the editorial review or the decision to publish this article. Swaminathan Sethuraman is an editorial board member for Bioactive Materials and was not involved in the editorial review or the decision to publish this article. All authors declare that there are no competing interests.

Acknowledgements

The authors wish to acknowledge Nano Mission, Department of Science & Technology (DST) (SR/NM/TP-83/2016 (G)), and Prof. T. R. Rajagopalan R & D Cell of SASTRA Deemed University for financial and infrastructural support. We also wish to acknowledge ATGC grant, Department of Biotechnology (DBT) (BT/ATGC/127/SP41147/2021), Adhoc funding, Indian Council of Medical Research (ICMR) (17x3/Adhoc/23/2022-ITR) and DST SERB CRG (Exponential Technologies) grant (CRG/2021/007847) for financial support.

Dr. Kumbar acknowledges the funding support provided by the National Institutes of Health (#R01NS134604, #R01EB034202, #R01AR078908, and #R01EB030060) and the U.S. Army Medical Research Acquisition Activity (USAMRAA) through the CDMRP Peer-Reviewed Medical Research Program (Award No. W81XWH2010321, PR230581, and HT94252410137).

Appendix A. Supplementary data

Supplementary data to this article can be found online at https://doi.org/10.1016/j.bioactmat.2024.10.028.

References

[1] R.M.G. Menorca, T.S. Fussell, J.C. Elfar, Nerve Physiology: mechanisms of injury and recovery, Hand Clin. 29 (3) (2013/08/01).

[2] M.C.O. Rodrigues, A.A. Rodrigues, L.E. Glover, J. Voltarelli, C.V. Borlongan, Peripheral nerve repair with cultured Schwann cells: getting closer to the clinics, Sci. World J. 2012 (1) (2012/01/01).

[3] B. Lopes, P. Sousa, R. Alvites, M. Branquinho, A.C. Sousa, C. Mendonça, L. M. Atayde, A.L. Luís, A.S.P. Varejão, A.C. Maurício, Peripheral nerve injury treatments and advances: one Health perspective, Int. J. Mol. Sci. 23 (2) (2022 Jan 14).

[4] W.Z. Ray, S.E. Mackinnon, Management of nerve gaps: autografts, allografts, nerve transfers, and end-to-side neurorrhaphy, Exp. Neurol. 223 (1) (2010/05/01).

[5] A. Zennifer, M. Thangadurai, D. Sundaramurthi, S. Sethuraman, Additive manufacturing of peripheral nerve conduits – fabrication methods, design considerations and clinical challenges, SLAS Technology 28 (3) (2023) 102–126.

[6] M. Anderson, N.B. Shelke, O.S. Manoukian, X. Yu, L.D. McCullough, S.G. Kumbar, Peripheral nerve regeneration strategies: electrically stimulating polymer based nerve growth conduits, Crit. Rev. Biomed. Eng. 43 (2–3) (2015).

[7] O.S. Manoukian, M.R. Arul, S. Rudraiah, I. Kalajzic, S.G. Kumbar, Aligned microchannel polymer-nanotube composites for peripheral nerve regeneration: small molecule drug delivery, J. Contr. Release 296 (2019) 54–67.

[8] O.S. Manoukian, S. Stratton, M.R. Arul, J. Moskow, N. Sardashti, X. Yu, S. Rudraiah, S.G. Kumbar, Polymeric ionically conductive composite matrices and electrical stimulation strategies for nerve regeneration: in vitro characterization, Journal of biomedical materials research. Part B, Applied biomaterials 107 (6) (2019) 1792–1805.

[9] J. Moskow, B. Ferrigno, N. Mistry, D. Jaiswal, K. Bulsara, S. Rudraiah, S. G. Kumbar, Review: bioengineering approach for the repair and regeneration of peripheral nerve, Bioact. Mater. 4 (2019) 107–113.

[10] W. Chang, M.B. Shah, G. Zhou, K. Walsh, S. Rudraiah, S.G. Kumbar, X. Yu, Polymeric nanofibrous nerve conduits coupled with laminin for peripheral nerve regeneration, Biomedical Materials 15 (3) (2020) 35003, 035003.

[11] B. Ferrigno, R. Bordett, N. Duraisamy, J. Moskow, M.R. Arul, S. Rudraiah, S. P. Nukavarapu, A.T. Vella, S.G. Kumbar, Bioactive polymeric materials and electrical stimulation strategies for musculoskeletal tissue repair and regeneration, Bioact. Mater. 5 (3) (2020) 468–485.

[12] O.S. Manoukian, J.T. Baker, S. Rudraiah, M.R. Arul, A.T. Vella, A.J. Domb, S. G. Kumbar, Functional polymeric nerve guidance conduits and drug delivery strategies for peripheral nerve repair and regeneration, J. Contr. Release 317 (2020) 78–95.

[13] E. Stocco, S. Barbon, A. Emmi, C. Tiengo, V. Macchi, R.D. Caro, A. Porzionato, E. Stocco, S. Barbon, A. Emmi, C. Tiengo, V. Macchi, R. De Caro, A. Porzionato, Bridging gaps in peripheral nerves: from current strategies to future perspectives in conduit design, Int. J. Mol. Sci. 24 (11) (2023-05-24) 9170, 2023, Vol. 24.

[14] X. Dong, Y. Yang, Z. Bao, A.C. Midgley, F. Li, S. Dai, Z. Yang, J. Wang, L. Liu, W. Li, Y. Zheng, S. Liu, Y. Liu, W. Yu, J. Liu, M. Fan, M. Zhu, Z. Shen, G. Xiaosong, D. Kong, Micro-nanofiber composite biomimetic conduits promote long-gap peripheral nerve regeneration in canine models, Bioact. Mater. 30 (2023/12/01).

[15] J. Wang, H. Xiong, T. Zhu, Y. Liu, H. Pan, C. Fan, X. Zhao, W.W. Lu, Bioinspired multichannel nerve guidance conduit based on shape memory nanofibers for potential application in peripheral nerve repair, ACS Nano 14 (10) (August 13, 2020).

[16] D. Park, D. Kim, S.J. Park, J.H. Choi, Y. Seo, D.-H. Kim, S.-H. Lee, J.K. Hyun, J. Yoo, Y. Jung, S.H. Kim, D. Park, D. Kim, S.J. Park, J.H. Choi, Y. Seo, D.-H. Kim, S.-H. Lee, J.K. Hyun, J. Yoo, Y. Jung, S.H. Kim, Micropattern-based nerve guidance conduit with hundreds of microchannels and stem cell recruitment for nerve regeneration, npj Regenerative Medicine 7 (1) (2022), 7(1) (2022-10-20).

[17] Y. Fang, C. Wang, Z. Liu, J. Ko, L. Chen, T. Zhang, Z. Xiong, L. Zhang, W. Sun, 3D printed conductive multiscale nerve guidance conduit with hierarchical fibers for peripheral nerve regeneration, Adv. Sci. 10 (12) (2023/04/01).

[18] C.R. Carvalho, W. Chang, J. Silva-Correia, R.L. Reis, J.M. Oliveira, J. Kohn, Engineering silk fibroin-based nerve conduit with neurotrophic factors for proximal protection after peripheral nerve injury, Adv. Healthcare Mater. 10 (2) (2021/01/01).

[19] C.R. Carvalho, J.M. Oliveira, R.L. Reis, Frontiers | modern trends for peripheral nerve repair and regeneration: beyond the hollow nerve guidance conduit, Front. Bioeng. Biotechnol. 7 (2019/11/22).

[20] Y. Fang, C. Wang, Z. Liu, J. Ko, L. Chen, T. Zhang, Z. Xiong, L. Zhang, W. Sun, 3D printed conductive multiscale nerve guidance conduit with hierarchical fibers for peripheral nerve regeneration, Adv. Sci. 10 (12) (2023).

[21] G.H. Borschel, K.F. Kia, W.M. Kuzon, R.G. Dennis, Mechanical properties of acellular peripheral nerve, J. Surg. Res. 114 (2) (2003/10/01).

[22] A. Piskin, B.Z. Altunkaynak, A. Çıtlak, H. Sezgin, O. Yazıcı, S. Kaplan, Immediate versus delayed primary nerve repair in the rabbit sciatic nerve, Neural Regeneration Research 8 (36) (2013 Dec 25).

[23] A. Zennifer, D.R. Chellappan, P. Chinnaswamy, A. Subramanian, D. Sundaramurthi, S. Sethuraman, Efficacy of 3D printed anatomically equivalent thermoplastic polyurethane guide conduits in promoting the regeneration of critical-sized peripheral nerve defects, Biofabrication 16 (4) (2024) 45015, 045015.

[24] M.-S. M`Bengue, T. Mesnard, F. Chai, M. Maton, V. Gaucher, N. Tabary, M.-J. García-Fernandez, J. Sobocinski, B. Martel, N. Blanchemain, M.-S. M'Bengue, T. Mesnard, F. Chai, M. Maton, V. Gaucher, N. Tabary, M.-J. García-Fernandez, J. Sobocinski, B. Martel, N. Blanchemain, Evaluation of a medical grade thermoplastic polyurethane for the manufacture of an implantable medical device:

the impact of FDM 3D-printing and gamma sterilization, Pharmaceutics 15 (2) (2023-01-30) 456, 2023, Vol. 15.

[25] D. Sundaramurthi, U.M. Krishnan, S. Sethuraman, Biocompatibility of poly(3-hydroxybutyrate-co3-hydroxyvalerate) (PHBV) nanofibers for skin tissue engineering, J. Biomed. Nanotechnol. 9 (8) (2013).

[26] J. Bai, J. Dai, G. Li, Electrospun composites of PHBV/pearl powder for bone repairing, Prog. Nat. Sci.: Mater. Int. 25 (4) (2015/08/01).

[27] A. Delavarde, G. Savin, P. Derkenne, M. Boursier, R. Morales-Cerrada, B. Nottelet, J. Pinaud, S. Caillol, Sustainable polyurethanes: toward new cutting-edge opportunities, Prog. Polym. Sci. 151 (2024/04/01).

[28] A. Zaszczynska, P. Sajkiewicz, A. Gradys, Piezoelectric scaffolds as smart materials for neural tissue engineering, Polymers 12 (1) (2020 Jan 8).

[29] S.G. Kumbar, R. James, S.P. Nukavarapu, C.T. Laurencin, S.G. Kumbar, R. James, S. P. Nukavarapu, C.T. Laurencin, Electrospun nanofiber scaffolds: engineering soft tissues, Biomedical Materials 3 (3) (2008-08-08).

[30] R. James, U.S. Toti, C.T. Laurencin, S.G. Kumbar, Electrospun nanofibrous scaffolds for engineering soft connective tissues, Methods Mol. Biol. 726 (2011) 243–258.

[31] D. Jaiswal, R. James, N.B. Shelke, M.D. Harmon, J.L. Brown, F. Hussain, S. G. Kumbar, Gelatin nanofiber matrices derived from schiff base derivative for tissue engineering applications, J. Biomed. Nanotechnol. 11 (11) (2015).

[32] B.K. Tarus, N. Fadel, A. Al-Oufy, M. El-Messiry, N.F. Bethwel K. Tarus, Affaf Al-Oufy, Magdi El-Messiry, Investigation of mechanical properties of electrospun poly (vinyl chloride) polymer nanoengineered composite, Journal of Engineered Fibers and Fabrics 15 (2020-12-20).

[33] M. Bragaglia, M. Mariani, C. Sergi, F. Sarasini, J. Tirillò, F. Nanni, Polylactic acid as biobased binder for the production of 3D printing filaments for Ti6Al4V alloy manufacturing via bound metal deposition, J. Mater. Res. Technol. 27 (2023/11/01).

[34] S. Hlaváčiková, L. Omaníková, V. Horváth, P. Alexy, V. Jančovičová, A. Baco, M. Mikolajová, M. Fogašová, K. Tomanová, J. Feranc, M. Ďurfina, P. Menčík, V. Melčová, R. Plavec, The possibility of using the regranulate of a biodegradable polymer blend based on polylactic acid and polyhydroxybutyrate in FDM 3D printing technology, Results in Materials 21 (2024/03/01).

[35] B. Zhang, L. Wang, P. Song, X. Pei, H. Sun, L. Wu, C. Zhou, K. Wang, Y. Fan, X. Zhang, 3D printed bone tissue regenerative PLA/HA scaffolds with comprehensive performance optimizations, Mater. Des. 201 (2021/03/01).

[36] R. Augustine, A. Hasan, Y.B. Dalvi, S.R.U. Rehman, R. Varghese, R.N. Unni, H. C. Yalcin, R. Alfkey, S. Thomas, A.-E.A. Moustafa, Growth factor loaded in situ photocrosslinkable poly(3-hydroxybutyrate-co-3-hydroxyvalerate)/gelatin methacryloyl hybrid patch for diabetic wound healing, Mater. Sci. Eng. C 118 (2021/01/01).

[37] P. Kuppan, K.S. Vasanthan, D. Sundaramurthi, U.M. Krishnan, S. Sethuraman, Development of poly(3-hydroxybutyrate-co-3-hydroxyvalerate) fibers for skin tissue engineering: effects of topography, mechanical, and chemical stimuli, Biomacromolecules 12 (2011) 3156–3165.

[38] V. Sharma, S.K. Dash, A. Manhas, J. Radhakrishnan, K. Jagavelu, R.S. Verma, Injectable hydrogel for co-delivery of 5-azacytidine in zein protein nanoparticles with stem cells for cardiac function restoration, Int. J. Pharm. 603 (2021/06/15).

[39] A. Subramanian, U.M. Krishnan, S. Sethuraman, A. Subramanian, U.M. Krishnan, S. Sethuraman, Fabrication of uniaxially aligned 3D electrospun scaffolds for neural regeneration, Biomedical Materials 6 (2) (2011-02-07).

[40] R. Dhandapani, P.D. Krishnan, A. Zennifer, V. Kannan, A. Manigandan, M.R. Arul, D. Jaiswal, A. Subramanian, S.G. Kumbar, S. Sethuraman, Additive manufacturing of biodegradable porous orthopaedic screw, Bioact. Mater. 5 (3) (2020/09/01).

[41] M.P. Sekar, P. Roopmani, U.M. Krishnan, Development of a novel porous polyvinyl formal (PVF) microfibrous scaffold for nerve tissue engineering, Polymer 142 (2018/04/25).

[42] D. Sundaramurthi, K.S. Vasanthan, P. Kuppan, U.M. Krishnan, S. Sethuraman, D. Sundaramurthi, K.S. Vasanthan, P. Kuppan, U.M. Krishnan, S. Sethuraman, Electrospun nanostructured chitosan–poly(vinyl alcohol) scaffolds: a biomimetic extracellular matrix as dermal substitute, Biomedical Materials 7 (4) (2012-05-08).

[43] M. Nune, U.M. Krishnan, S. Sethuraman, PLGA nanofibers blended with designer self-assembling peptides for peripheral neural regeneration, Mater. Sci. Eng. C 62 (2016/05/01).

[44] M. Nune, A. Subramanian, U.M. Krishnan, S.S. Kaimal, S. Sethuraman, Self-assembling peptide nanostructures on aligned poly(lactide-co-glycolide) nanofibers for the functional regeneration of sciatic nerve, Nanomedicine 12 (3) (2017-2-1).

[45] H. Jiang, X. Wang, X. Li, Y. Jin, Z. Yan, X. Yao, W.-E. Yuan, Y. Qian, Y. Ouyang, A multifunctional ATP-generating system by reduced graphene oxide-based scaffold repairs neuronal injury by improving mitochondrial function and restoring bioelectricity conduction, Materials Today Bio 13 (2022/01/01).

[46] J. Xu, Z. Lei, S. Liu, J. Chen, G. Gong, X. Cai, Z.L. Jun Xu, Sihan Liu, Jiayi Chen, Genghao Gong, Xiaofeng Cai, Preparation and characterization of biodegradable electrospinning PHBV/PBAT/TiO2 antibacterial nanofiber membranes, Journal of Engineered Fibers and Fabrics 17 (2022-12-08).

[47] Q. Wang, J. Ma, S. Chen, S. Wu, Q. Wang, J. Ma, S. Chen, S. Wu, Designing an innovative electrospinning strategy to generate PHBV nanofiber scaffolds with a radially oriented fibrous pattern, Nanomaterials 13 (7) (2023-03-23) 1150, 2023, Vol. 13.

[48] B. Thapsukhon, D. Daranarong, P. Meepowpan, N. Suree, R. Molloy, K. Inthanon, W. Wongkham, W. Punyodom, Effect of topology of poly(L-lactide-co-ε-caprolactone) scaffolds on the response of cultured human umbilical cord Wharton's jelly-derived mesenchymal stem cells and neuroblastoma cell lines, J. Biomater. Sci. Polym. Ed. 25 (10) (2014-7-3).

[49] M.M. Ghobashy, Z.I. Abdeen, Radiation crosslinking of polyurethanes: characterization by FTIR, TGA, SEM, XRD, and Raman spectroscopy, Journal of Polymers (1) (2016/01/01), 2016.

[50] T. Pulingam, J.N. Appaturi, T. Parumasivam, A. Ahmad, K. Sudesh, T. Pulingam, J. N. Appaturi, T. Parumasivam, A. Ahmad, K. Sudesh, Biomedical applications of polyhydroxyalkanoate in tissue engineering, Polymers 14 (11) (2022-05-24) 2141, 2022, Vol. 14.

[51] Z. Fang, Y. Xiao, X. Geng, L. Jia, Y. Xing, L. Ye, Y. Gu, A.-y. Zhang, Z.-g. Feng, Fabrication of heparinized small diameter TPU/PCL bi-layered artificial blood vessels and in vivo assessment in a rabbit carotid artery replacement model, Biomater. Adv. 133 (2022/02/01).

[52] B. Jin, Y. Yu, X. Chen, Y. Yang, Y. Xiong, Y.J. Im, Y. Zhao, J. Xiao, Microtubes with gradient decellularized porcine sciatic nerve matrix from microfluidics for sciatic nerve regeneration, Bioact. Mater. 21 (2023/03/01).

[53] S. Yang, J. Zhu, C. Lu, Y. Chai, Z. Cao, J. Lu, Z. Zhang, H. Zhao, Y.-Y. Huang, S. Yao, X. Kong, P. Zhang, X. Wang, Aligned fibrin/functionalized self-assembling peptide interpenetrating nanofiber hydrogel presenting multi-cues promotes peripheral nerve functional recovery, Bioact. Mater. 8 (02/01) (2022).

[54] Y. Guan, Z. Ren, B. Yang, W. Xu, W. Wu, X. Li, T. Zhang, D. Li, S. Chen, J. Bai, X. Song, Z. Jia, X. Xiong, S. He, C. Li, F. Meng, T. Wu, J. Zhang, X. Liu, H. Meng, Y. Wang, Dual-bionic regenerative microenvironment for peripheral nerve repair, Bioact. Mater. 26 (2023/08/01).

[55] D.V. Krishna, M.R. Sankar, Engineered approach coupled with machine learning in biofabrication of patient-specific nerve guide conduits - review, Bioprinting 30 (2023/04/01).

[56] G. Hussain, J. Wang, A. Rasul, H. Anwar, M. Qasim, S. Zafar, N. Aziz, A. Razzaq, R. Hussain, J.-L.G. de Aguilar, T. Sun, Current status of therapeutic approaches against peripheral nerve injuries: a detailed story from injury to recovery, Int. J. Biol. Sci. 16 (1) (2020) 116–134.

[57] M.F. Meek, K. Jansen, Two years after in vivo implantation of poly(DL-lactide-ε-caprolactone) nerve guides: has the material finally resorbed? J. Biomed. Mater. Res. 89A (3) (2009/06/01).

[58] M.J.O.E. Bertleff, M.F. Meek, J.-P.A. Nicolai, A prospective clinical evaluation of biodegradable neurolac nerve guides for sensory nerve repair in the hand, J. Hand Surg. 30 (3) (2005/05/01).

[59] M. Wang, X. Xiang, Y. Wang, Y. Ren, L. Yang, Y. Zhang, Comparison of tensile properties and knot security of surgical sutures: an in vitro mechanical study, J. Oral Maxillofac. Surg. 80 (7) (2022/07/01).

[60] S. Rotshenker, S. Rotshenker, Wallerian degeneration: the innate-immune response to traumatic nerve injury, J. Neuroinflammation 8 (1) (2011-08-30), 2011 8:1.

[61] C. Vyas, G. Ates, E. Aslan, J. Hart, B. Huang, P. Bartolo, Three-dimensional printing and electrospinning dual-scale polycaprolactone scaffolds with low-density and oriented fibers to promote cell alignment, 3D Print. Addit. Manuf. 7 (3) (2020 Jun 5).

[62] Q. Quan, H.-Y. Meng, B. Chang, G.-B. Liu, X.-Q. Cheng, H. Tang, Y. Wang, J. Peng, Q. Zhao, S.-B. Lu, Aligned fibers enhance nerve guide conduits when bridging peripheral nerve defects focused on early repair stage, Neural Regeneration Research 14 (5) (2019 May).

[63] J. Xu, Z. Lei, S. Liu, J. Chen, G. Gong, X. Cai, Preparation and characterization of biodegradable electrospinning PHBV/PBAT/TiO 2 antibacterial nanofiber membranes, Journal of Engineered Fibers and Fabrics 17 (2022) 155892502211365, 155892502211365.

[64] N.A. Tagandurdyyeva, M.A. Trube, I.O. Shemyakin, D.N. Solomitskiy, G. V. Medvedev, E.N. Dresvyanina, Y.A. Nashchekina, E.M. Ivan'kova, I. P. Dobrovol'skaya, A.M. Kamalov, E.G. Sukhorukova, O.A. Moskalyuk, V.E. Yudin, Properties of resorbable conduits based on poly(L-lactide) nanofibers and chitosan fibers for peripheral nerve regeneration, Polymers 15 (15) (2023) 3323, 3323.

[65] E. Biazar, S.H. Keshel, M. Pouya, Efficacy of nanofibrous conduits in repair of long-segment sciatic nerve defects, Neural Regeneration Research 8 (27) (2013 Sep 25).

[66] R.D. Fields, Myelin Formation and remodeling, Cell 156 (1) (2014/01/16).

[67] O.S. Manoukian, S. Rudraiah, M.R. Arul, J.M. Bartley, J.T. Baker, X. Yu, S. G. Kumbar, Biopolymer-nanotube nerve guidance conduit drug delivery for peripheral nerve regeneration: in vivo structural and functional assessment, Bioact. Mater. 6 (9) (2021/09).

[68] W. Wu, Y. Dong, H. Liu, X. Jiang, L. Yang, J. Luo, Y. Hu, M. Gou, 3D printed elastic hydrogel conduits with 7,8-dihydroxyflavone release for peripheral nerve repair, Materials Today Bio 20 (2023/06/01).

[69] C. Xue, H. Zhu, H. Wang, Y. Wang, X. Xu, S. Zhou, D. Liu, Y. Zhao, T. Qian, Q. Guo, J. He, K. Zhang, Y. Gu, L. Gong, J. Yang, S. Yi, B. Yu, Y. Wang, Y. Liu, Y. Yang, X. Gu, Skin derived precursors induced Schwann cells mediated tissue engineering-aided neuroregeneration across sciatic nerve defect, Bioact. Mater. 33 (2024/03/01).